Search for relic neutrinos from past supernovae in Super-Kamiokande

Mikio Morii

February, 2001

Master's thesis

High Energy Experimental Physics Group
Department of Physics
Tokyo Institute of Technology
O-okayama, Meguro, Tokyo 152-8551, Japan

Abstract

The SN relic neutrinos from the past supernovae are searched, using a 78 kt·year exposure of the Super-Kamiokande detector. To find positron events produced by the SN relic neutrinos, we reject contaminating muon events and the spallation background induced by the energetic cosmic-ray muons. Finally, 138 electron events are selected in the energy range between 20 and 80MeV. The amount of the atmospheric neutrino backgrounds, especially the decay electrons from the invisible muon events, are estimated by a Monte Carlo simulation. The 90% confidence level total flux limit of the $\bar{\nu_e}$ SN relic neutrinos is obtained to be $F_\nu < 231(\mathrm{cm}^{-2}\mathrm{sec}^{-1})$, which is the best value, so far obtained.

Acknowledgments

First of all, I would like to express my deep gratitude to Prof. Y.Watanabe for giving me the chance to participate in this great experiment and giving me an excellent guidance and heartful encouragement. I would like to express sincere appreciation to Prof. T.Tanimori and Prof. A.Bondar for his suggestive advice. I also thank Prof. K.Kaneyuki and Dr. H.Ishino for teaching me from the fundamental part of the experiment and Dr. H.Kubo and Dr. B.Cheon for useful suggestions.

I would like to show my great gratitude to all of the collaborators of the Super-Kamiokande experiment for their hard work in construction and operation of the experiment. In particular, I would like to thank Prof. Y.Totsuka for his competence in leading the Super-Kamiokande experiment. I would like to show my appreciation to Prof. Y.Suzuki for his useful suggestions, support and leadership for the solar neutrino and supernova neutrino analysis group.

I am grateful to Dr. Y.Fukuda and Mr. M.Malek, with whom I disccussed about the SN relic neutrinos on many occasions, and then I could comprehend deeply on these neutrinos.

I am really thankful to Dr. T.Totani for telling me his calcuration of the SN relic neutrinos, which plays crucial role in this thesis.

I am also grateful to members of the analysis group: Prof. M.Nakahata, Dr. Y.Takeuchi, Dr. Y.Koshio, Prof. R.Svoboda, Prof. K.Martens, Dr. M.Vagins, Dr. M.Smy, Dr. G.Gullian, Dr. D.Liu, Messrs. N.Sakurai, and J.Yoo for a lot of helpful discussions. I am thankful to Prof. T.Kajita, Prof. A.Okada, Prof. Y.Itow, Prof. K.Inoue, Prof. J.Shirai, Prof. K.Miyano, Prof. Y.Nagashima, Prof. M.Takita, Prof. K.Nishijima, Prof. Tasaka, Prof. M.Sakuda, Dr. M.Miura, Dr. M.Shiozawa, Dr. S.Moriyama, Dr. Y.Obayashi, Dr. T.Toshito, Dr. K.Ishihara, Dr. Y.Hayato, Dr. A.T.Suzuki, Dr. H.Okazawa, Dr. T.Ishizuka, Dr. T.Inagaki, Prof. R.W.Ellsworth, Dr. C.Yanagisawa, Dr. Matsuno, Dr. S.Kate, Dr. T.Barszczak, Dr. C.Mauger, Messrs. and Mses. M.Etoh, T.Maruyama, A.Kibayashi, H.Kim, J.Kameda, K.Kobayashi, S.Nakayama, S.Yamada, C.Saji, M.Takahashi, S.Inaba, M.Kirisawa, H.Takeuchi, M.Koike, Y.Hatakeyama, and K.Nitta for their kind suggestions. I thankful to Dr. S.Sato, Messrs. K.Miuchi and H.Sekiya.

I really thankful to wonderful colleagues: S.Fukuda, Y.Gando, Y.Iimori, Y.Ichikawa, M.Ishitsuka, Y.Kajiyama, and C.Mitsuda, with whom I really enjoyed heartful Kamioka life. On many occasion we discussed, helped, encouraged and enjoyed one another.

I thank to the technical staff Messrs. K.Yokokawa, and T.Furuta, and also the members of Kamioka dormitory staffs, and the secretaries in Kenkyutou. I respect Mr. Katayama. I will never forget the late Prime Minister K.Obuchi of blessed memory, who visited Kamioka site and encouraged us. I gratefully acknowledge the cooperation of the Kamioka Mining and Smelting Company. The Super-Kamiokande experiment was built from, and has been operated with, funding by the Japanese Ministry of Education, Science, Sports and Culture, and the United

States Department of Energy.

Finally, I greatly appreciate the members of Watanabe-Tanimori Laboratory: Dr. Y.Oshima, Dr. A.Ochi, Dr. K.Sakurazawa, Dr. S.Ichizawa, Dr. Y.Nishi, Dr. M.Moriya, Dr. H.Muraishi, Messrs. and Mses. H.Kakuno, J.Kaneke, S.Hara, M.Ohta, T.Futagami, H.Fujiyasu, J.Kushida, A.Namekata, A.Asahara, T.Hirai, K.Takano, T.Nakamura, T.Nagayoshi, S.Koishi, H.Nishihama, S.Yanaka, R.Orito, T.Ooyabu, M.Shirahata, R.Nishimura, and A.Ohno for their kind suggestions and supports.

Contents

List of Figures

List of Tables

Chapter 1

Introduction

A supernova is an intensive explosion of a massive star, occurring when it is dying. It shines suddenly as bright as a galaxy. This explosion is the most energetic in the universe as far as we know[1]. When a supernova explode, enormous number of neutrinos are emitted. It is called *neutrino burst*. In fact such a neutrino burst was observed for SN1987A in Large Magellanic Cloud on 23 February 1987 by KAMIOKANDE-II and IMB neutrino detectors[1, 2, 3]. Since the birth of the universe, innumerable supernovae have occurred and enormous number of neutrinos have been emitted. So, neutrinos originating from past supernovae must constitute the cosmic background neutrinos. We call them the *SN relic neutrinos*[2]. The detection of the SN relic neutrinos will provide us valuable information on the history of the supernova rate and hence the evolution of galaxies, as well as the properties of the supernova neutrinos.

The SN relic neutrinos have not ever observed, yet. Many researchers estimate its flux and energy spectrum. The predicted total neutrino flux varies in the range 1-100 cm^{-2}sec^{-1} [4–16]. So far, the upper limit for the total flux is 780(cm^{-2}sec^{-1}) at 90 % confidence level, obtained by the KAMIOKANDE-II experiment in 1991[17, 18].

A search for the SN relic neutrinos are described in this thesis, using a water Cherenkov detector, Super-Kamiokande, which is the only detector in the world that can improve this upper limit. The most serious problem in the observation of the SN relic neutrinos is to exclude other backgrounds. Figure 1.1 shows the SN relic neutrino flux expected, and those for other neutrinos. The energy range 10-50 MeV is the range to look for the SN relic neutrinos, because lower side and upper side are hidden by reactor neutrinos and atmospheric neutrinos, respectively. Although there are the solar neutrinos in the range less than 20 MeV, these neu-

---

[1] *Gamma ray burst* may be more energetic phenomenon than supernova. Its true mechanism has not be revealed and been mysterious, yet.

[2] When the cosmic temperature become $T = 0.72MeV$, neutrinos decoupled from the thermal equilibrium and the universe become clear for the neutrinos. This neutrino constitute the cosmic background neutrinos and its temperature is $T = 1.92K$, now. It is also called the relic neutrinos. To distinguish them we call the relic neutrinos originating from the past supernovae the SN relic neutrinos.

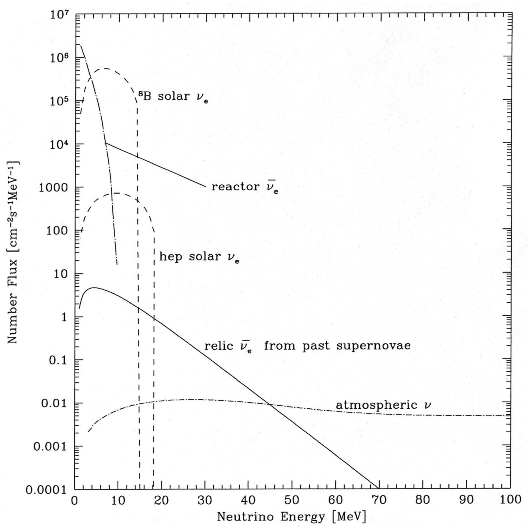

Figure 1.1: The expected neutrino flux from many sources, extracted from [9]

trinos are ν_e's, then the direction of recoil electrons in the detector is strongly concentrated to the opposite direction of the Sun. Therefore, the solar neutrinos are an avoidable background. However, *spallation* background exists in range less than 20 MeV, which is hard to be avoided and estimation of amount of this is also hard. So, the range 20-50 MeV are searched for the SN relic neutrinos in this thesis.

The theories related to the SN relic neutrinos, the reactions of those neutrinos in water, and expected backgrounds are described in Chapter 2. The details of the Super-Kamiokande detector used for the SN relic neutrino search are explained in Chapter 3. Various calibrations for the detector are shown in Chapter 4. The reconstruction methods of the neutrino events are delineated in Chapter 5. The reduction methods of the data are described in Chapter 6. The Monte Carlo simulations used in the Super-Kamiokande experiment are detailed in Chapter 7. The backgrounds from the atmospheric neutrinos are analyzed in Chapter 8. The real events after the reduction and the corresponding Monte Carlo events are compared. Finally, the total flux of the SN relic neutrino are obtained in Chapter 9. The conclusion in this thesis and the prospects to discover the SN relic neutrino are mentioned in Chapter 10.

Chapter 2

Theory

In this chapter, theories related to the SN relic neutrinos are described.

2.1 Evolution of a star

A star is born in the cloud of gas, which is composed of hydrogen, helium mainly, and other massive elements, contracting itself by gravity. In this process, the energy of gravity is released as a thermal energy, so the center of a star becomes high temperature. When its temperature reaches about 2×10^7 K, the nuclear fusion of hydrogens starts and the star begins to shine. When hydrogens are consumed at the stellar center, the core of helium contracts to increase temperature further and are ignited as a new fuel. This process proceeds from one element to another. In each step when the temperature at stellar core does not reach at the ignition point of a new fuel, the electrons in the stellar core degenerate and the nuclear burning stops. Such difference is caused by the difference of the mass of a star. When the mass of a star is large enough, the star eventually evolves into the *onion-skin* structure as shown in Figure 2.1, where the core is made of the most stable element, Fe.

2.2 Death of a star

As mentioned above, depending on the mass of a star, its evolution is different, and also the death of a star is different. Moreover it also depend on whether a star is singlet or binary.

In a single star case, its evolution and death are shown in [19, 20]:

1. $M < 0.08 M_\odot$[1]: When a proto-star contracts itself by gravity, electrons degenerate before ignition of hydrogens, because its mass is too small. Then this becomes a brown dwarf or a Jupiter-like star.

[1] $M_\odot$ is the mass of the sun

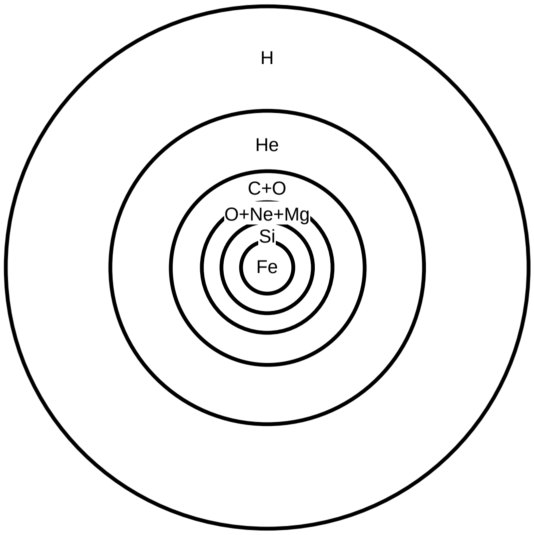

Figure 2.1: The onion-skin structure of the massive star with $M > 10M_\odot$, just before the gravitational collapse.

2. $0.08M_\odot < M < 0.45M_\odot$: After hydrogen burning, electrons degenerate in He core. Then this becomes a He white dwarf[2].

3. $0.45M_\odot < M < 7M_\odot$: After helium burning, electrons degenerate in C+O core. The outer layer of the star escapes and expands from the star, and then form a planetary nebula, on the other hand, the inner core becomes the C+O white dwarf.

4. $7M_\odot < M < 8M_\odot$: After He burning electrons degenerate in C+O core. If temperature of the center becomes 3×10^8K, C ignites in C+O core where electrons degenerate. If degenerated core ignite, nuclear reaction rushes, and the star explode. It is called *thermonuclear supernova explosion.*

5. $8M_\odot < M < 10M_\odot$: In the center of the star a O+Ne+Mg core is formed. This is supported by the pressure of the electron degeneration. When the Fermi energy of electrons becomes higher than the threshold energy of the electron capture reactions, these reactions proceed and the pressure of the electron degeneration decreases because of the decrease of the electrons. Then the stellar core collapse by the gravity itself, and results in the *collapse-driven supernova explosion.* After a supernova explosion a neutron star is left in its center.

6. $10M_\odot < M < 40 \pm 10M_\odot$: This type of stars evolves up to the structure like Figure 2.1, where a Fe core exists in the center of this. This is also supported by the pressure of the

[2]The white dwarf is a small and high temperature star supported by the pressure of the electron degeneration. The white dwarf shines by emission of thermal energy and becomes gradually cool and dark.

electron degeneration. When the temperature of the core exceeds about 5×10^9K, the photo-dissociation of nuclei such as

$$^{56}Fe + \gamma \to 13^4He + 4n - 124.4\text{MeV} \tag{2.1}$$

occurs. Because this is an endothermic reaction, the core cannot support itself and collapses. It also results in the collapse-driven supernova explosion. After this explosion a neutron star is left in its center.

7. $40 \pm 10M_\odot < M$: This doom is the same as the case of $10M_\odot < M < 40 \pm 10M_\odot$, but in the gravitational collapse, a supernova explosion cannot occur and becomes a black hole.

In the binary star case, the evolution process is more complicated. Details are described in [20].

2.3 Types of Supernovae

Supernovae are classified into two types: type I and type II. In their spectra, the type I does not have hydrogen line while the type II has. Each type is divided into subclasses. Figure 2.2 shows types of supernovae. The type I is the explosion of a star which has lost the hydrogen layer, and mostly is the rush of the carbon nuclear fusion reaction of a white dwarf in the binary system. On the other hand, the type II is the explosion of a massive star with hydrogen layer, which is caused by the gravitational collapse of its core. But there is the type I supernova caused by gravitational collapse, then when we consider the mechanism of supernova, it is appropriate that supernovae are classified into two types: thermonuclear supernova and collapse-driven supernova. The former do not emit neutrinos so much, the latter emit enormous number of neutrinos by which the star releases 99% of the gravitational energy.

2.4 Collapse-driven supernova explosion and neutrino burst

The dynamics of the supernova explosion and the neutrino burst is as follows and Figure 2.3 shows schematic view of this process [21, 19, 20].

1. Onset of collapse: As the core (O+Ne+Mg or Fe) of a massive star approaches the Chandrasekhar limit, it becomes unstable owing to two processes; electron capture and nuclear photo-dissociation. A relatively less massive core becomes unstable by the former process at first and a hot massive core, mainly by the latter. When the density and the temperature increase with the core collapse, the two processes cooperate. ν_es are produced by electron capture on nuclei, that is, by the reaction, $e^- A \to \nu_e A'$. ν_es escape freely from the core.

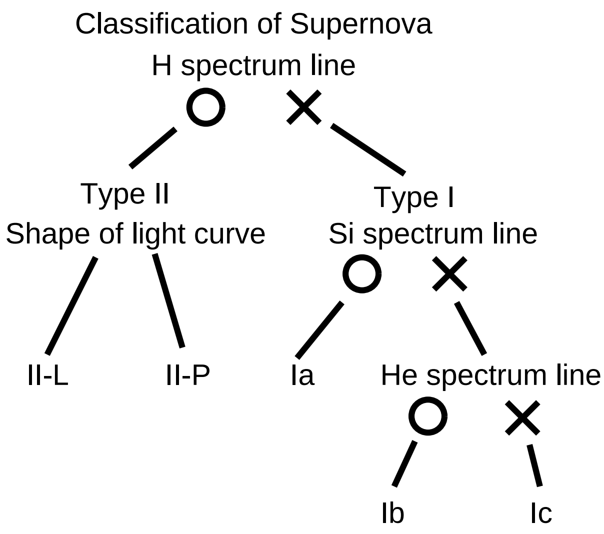

Figure 2.2: The classification of the supernova: The supernovas are classified into type I or type II. Type II is classified into Type II-P or Type II-L, where Type II-P has a plateau phase in its light curve, Type II-L has a linearly declining light curve. Type I is classified as shown in this figure, depending on whether Si and He spectrum lines exist or not.

2. Neutrino trapping: The dominant opacity source for ν_es during the collapse stage is coherent scattering off nuclei, $\nu_e A \rightarrow \nu_e A$, cross section of which is proportional to A^2, because the wave length of neutrinos are longer than the size of nuclei. In the collapse stage, only ν_es are emitted copiously by electron capture. Although ν_es can escape freely from the core at first, when the neutrino mean free path becomes shorter than the core size and the core becomes opaque to neutrinos, the *neutrinosphere* appears in the core as a surface which could be seen by neutrino telescopes. Furthermore when the neutrino diffusion time becomes longer than the core's dynamical time scale, neutrinos become unable to escape from the core in the collapse stage and can be regarded as trapped.

3. Core bounce and shock wave formation: When the central density exceeds the nuclear density, the EOS[3] stiffens suddenly because of the hard component of the nuclear force. The subsonically falling inner core bounces simultaneously; there is a stable hydrostatic configuration for the inner core and, when the inner core contracts beyond this equilibrium configuration due to the inertia, it bounces back to be the equilibrium configuration like a spring. A pressure wave originated from the center grows to be a shock wave near the boundary between the inner core and the supersonically falling outer core.

[3] In general, when the density of the matter increase, the pressure also increase. The state that the ratio of the increase of the pressure to the increase of the density is large is said that the EOS (Equation Of the State) is stiffen, The opposite state is said that the EOS is soft.

4. Neutronization burst: The shock wave propagates into the outer core with dissociating nuclei into free nucleons, because the shocked region behind the shock wave become high temperature($\sim$ 10MeV). Since the cross section of electron capture on free protons is larger than that on nuclei, a large amount of ν_es are produced in the shocked region by the reaction $e^- p \rightarrow \nu_e n$. Further the emitted ν_es can escape freely because the opacity caused by coherent scattering off nuclei become small. Thus the burst of ν_es occurs. it is called *neutronization burst.* Its time scale and emitted energy are 10 msec and 10^{51} erg.

5. Matter accretion into the protoneutron star and core explosion: Since the shocked region is hot ($T \gtrsim O(10)$MeV) and relatively low density, the electron degeneracy is not high and relativistic positrons are also created thermally. Neutrinos other than ν_es are emitted via reactions $e^+ n \rightarrow \bar{\nu_e} p$, $e^+ e^- \rightarrow \nu\bar{\nu}$ and they carry out the thermal energy of shocked matter as well as ν_es produced via $e^- p \rightarrow \nu_e n$. A part of shocked outer core accretes onto the hydrostatic protoneutron star and the released gravitational energy is converted into thermal energy and emitted as thermal neutrinos. This accretion phase might last only $O(10)$msec for the case of prompt explosion while it might last long ($O(1)$sec) for the case of delayed explosion.

6. Cooling stage of the protoneutron star: A protoneutron star cools down and deleptonize to a normal neutron star emitting thermal neutrinos, whose energy is $\sim 10^{53}$erg, in the time scale $O(10)sec$.

7. Supernova explosion: After several hours from the core bounce, the shock wave reaches the stellar surface and the star actually explodes. A neutron star bas been already formed in the center.

Figure 2.4 shows time profile of the neutrino burst.

Almost same energy is carried off by each species of neutrinos, and the total energy carried by all kinds of neutrinos is about 3×10^{53}erg. The mean energies of the neutrinos are $E_{\nu_e} = 10$MeV, $E_{\bar{\nu_e}} = 15$MeV, and $E_{\nu_\mu} = E_{\bar{\nu_\mu}} = E_{\nu_\tau} = E_{\bar{\nu_\tau}} = 20$MeV.

2.5 Energy spectrum of neutrinos emitted from a supernova

However the mechanism of supernova explosion is complicated, it is known that emergent neutrino spectra can be often fitted by the Fermi-Dirac spectra with non-zero chemical potential[19]:

$$\frac{dN_\nu(E)}{dE} = \frac{c}{4}\frac{4\pi}{(2\pi\hbar c)^3}\frac{E^2}{e^{(E-\mu)/T}+1}4\pi R^2, \tag{2.2}$$

where the parameters, T, μ, and R are the temperature, the chemical potential, and radius. Figure 2.5 shows the energy spectrum of anti-electron neutrinos from a supernova.

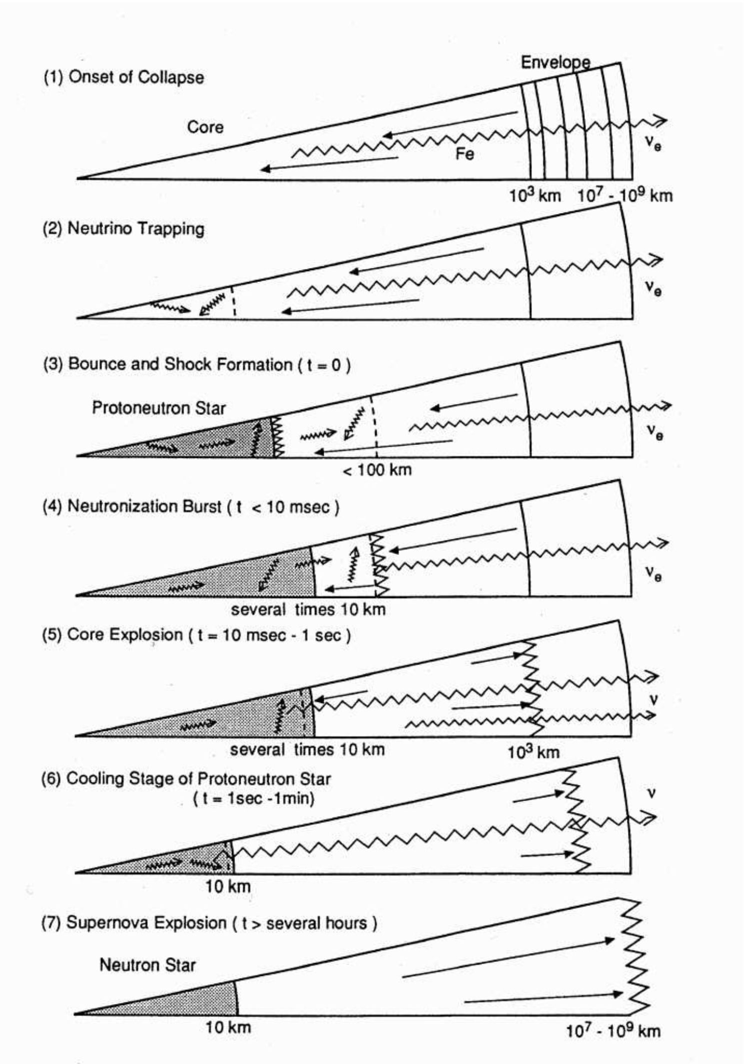

Figure 2.3: Collapse-driven supernova explosion and neutrinos. Dashed arc represents the neutrinosphere and waved arc represents the shock front. Shaded region is the protoneutron star which has been in hydrostatic configuration. Solid arrow represents the matter motion and waved arrow represents neutrinos. This figure is extracted from [19].

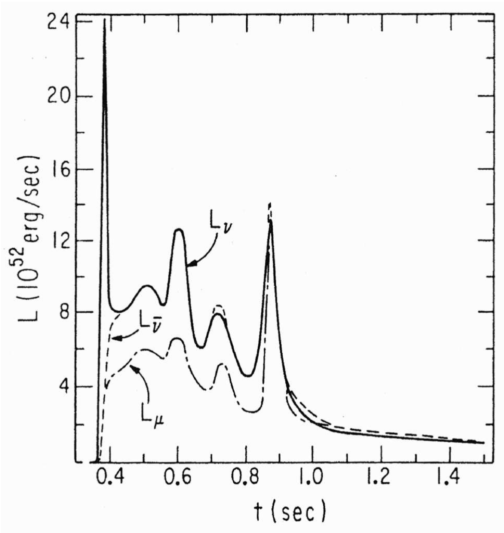

Figure 2.4: Evolution of the neutrino luminosity in a case of the delayed explosion, extracted from [22]. Solid line is ν_e, dashed line is $\bar{\nu}_e$ and dot-dashed line is $\nu_\mu, \bar{\nu_\mu}, \nu_\tau, or \bar{\nu_\tau}$. The neutronization burst peak of ν_e is drawn one-half its actual height. (The actual peak luminosity is about 5×10^{53}erg/sec.)

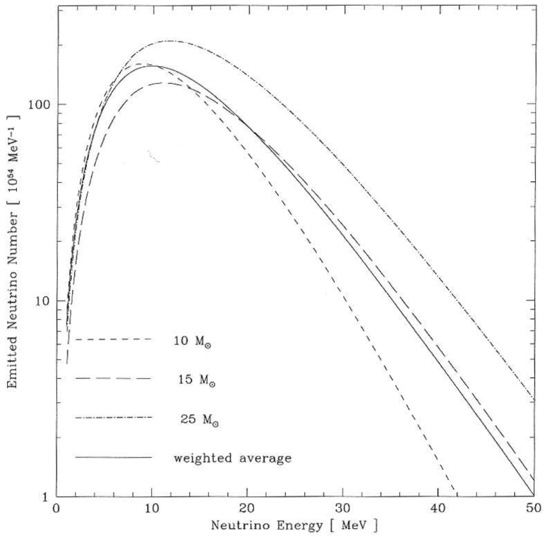

Figure 2.5: The energy spectrum of anti-electron neutrinos from a supernova, extracted from [9].

2.6 Cosmology

The assumption that the matter (star, galaxy) distribution in the universe is homogeneous and isotropical is called *cosmological principle*, it is true in vast scale (≥ 100 Mpc) observationally.

The most general space-time metric for a homogeneous, isotropic space is the Friedmann-Robertson-Walker metric :

$$ds^2 = c^2 dt^2 - R(t)^2 \left[\frac{dr^2}{1 - kr^2} + r^2 (d\theta^2 + \sin^2 \theta d\phi^2) \right]. \tag{2.3}$$

$R(t)$ is the scale factor for distances in the comoving coordinates. With appropriate rescaling of the coordinates, k can be chosen to be $+1$, -1, or 0, corresponding to closed, open, or spatially flat geometries.

In expanding universe, the wavelength of light emitted from a distant source is shifted towards the red. From the metric (2.3), the ratio of the detected wavelength (λ) to emitted (laboratory) wavelength (λ_e) is given that:

$$1 + z \equiv \frac{\lambda}{\lambda_e} = \frac{R_0}{R_e} \tag{2.4}$$

where R_e and R_0 is the value of the scale factor at the time the light was emitted and at the present time[4], z is called the redshift parameter.

Assuming that the universe is composed of perfect fluid, and using the Friedmann-Robertson-Walker metric, the $(0, 0)$ component of the Einstein's equation[5] becomes

$$H^2 = \left(\frac{\dot{R}}{R} \right)^2 = \frac{8\pi G}{3} \rho - \frac{k}{R^2} c^2 + \frac{\Lambda}{3} c^2, \tag{2.6}$$

and the spatial component becomes

$$2\frac{\ddot{R}}{R} + \left(\frac{\dot{R}}{R} \right)^2 + \frac{k}{R^2} c^2 = -8\pi G \frac{p}{c^2} + \Lambda c^2. \tag{2.7}$$

Those are called the *Friedmann equations*. The energy conservation condition becomes

$$\frac{d}{dt}(\rho c^2 R^3) + p \frac{d}{dt} R^3 = 0. \tag{2.8}$$

Because the universe has become the matter-dominant since the early stage, using the matter-dominant condition $p = 0$, (2.8) becomes

$$\rho R^3 = \rho_0 R_0^3, \tag{2.9}$$

[4] In this and the next section, the subscript 0 means that the value is the one at the present time.

[5]

$$R_{\mu\nu} - \frac{1}{2} R g_{\mu\nu} = \frac{8\pi G}{c^4} T_{\mu\nu} + \Lambda g_{\mu\nu} \tag{2.5}$$

then

$$\rho = \rho_0 \frac{R_0^3}{R^3} = \rho_0 (1+z)^3. \tag{2.10}$$

Using (2.6) and (2.10),

$$\dot{z} = -(1+z) H_0 \sqrt{(1+z)^2(\Omega_0 z + 1) - \lambda_0 (z^2 + 2z)} \tag{2.11}$$

is derived, where $\Omega_0 = \frac{8\pi G}{3H_0^2}\rho_0$ and $\lambda_0 = \frac{\Lambda c^2}{3H_0^2}$.

2.7 SN relic neutrinos

The features of the SN relic neutrinos are as follows:

1. The SN relic neutrinos are the diffused neutrinos, which are coming from all directions at all time.
2. The SN relic neutrinos are composed of all species of neutrinos $\overset{(-)}{\nu}_e$, $\overset{(-)}{\nu}_\mu$, $\overset{(-)}{\nu}_\tau$, and the numbers are almost the same, because the neutrinos from a supernova have such features.
3. The SN relic neutrino spectrum is the superposition of the Fermi-Dirac spectra of all the past supernovae influenced by the red-shift effect and the supernova rate history, etc.

The flux of the SN relic neutrinos is calculated as follows. The differential number flux of the SN relic neutrinos at the present time t_0 is expressed by

$$\frac{dF_R(E)}{dE} = c\frac{dn_R(E)}{dE}, \tag{2.12}$$

where $\frac{dn_R(E)}{dE}$ is the present differential number density of the SN relic neutrinos.

Because of the red-shift, a neutrino whose energy is E' at the past cosmic time t' is observed that its energy is $E = E'/(1+z)$ at the present time, where z is the red-shift parameter.

The contribution to the present differential number density of the SN relic neutrinos in the energy interval of $E \sim E + \Delta E$ from the past supernovae at the cosmic time $t' \sim t' + \Delta t'$ is written as:

$$\frac{1}{(1+z)^3} R_{\rm SN}(t') n_{\rm G}(t') \frac{dN_\nu[E(1+z)]}{dE}(1+z)\Delta E \Delta t' \tag{2.13}$$

where $1/(1+z)^3$ denotes the volume expansion effect, $R_{\rm SN}(t')$, $n_{\rm G}(t')$, and $\frac{dN_\nu(E)}{dE}$ are the supernova rate per year per galaxy, the number density of galaxies, and the differential number flux of neutrinos emitted from a supernova.

Then, the present differential number density of the SN relic neutrinos is given by:

$$\begin{aligned}
\frac{dn_R(E)}{dE} &= \int_{t_{min}}^{t_0} \frac{1}{(1+z)^3} R_{\rm SN}(t') n_{\rm G}(t') \frac{dN_\nu[E(1+z)]}{dE}(1+z) dt' && (2.14)\\
&= \int_{t_{min}}^{t_0} R_{\rm SN}(t') n_{\rm G}(t_0) \frac{dN_\nu[E(1+z)]}{dE}(1+z) dt' && (2.15)\\
&= \int_{z_{max}}^{0} R_{\rm SN}(t') n_{\rm G}(t_0) \frac{dN_\nu[E(1+z)]}{dE}(1+z) \frac{dt'}{dz} dz && (2.16)
\end{aligned}$$

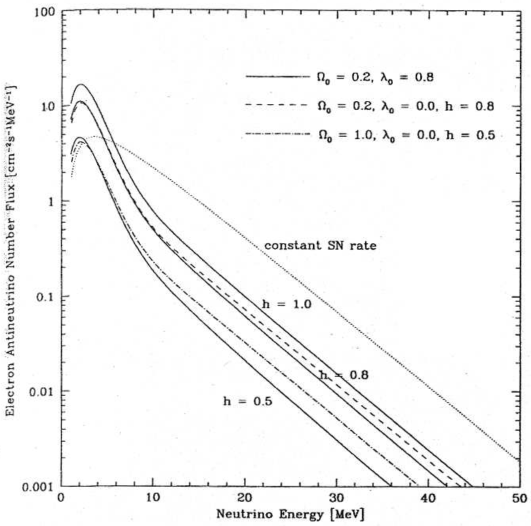

Figure 2.6: Energy spectra of the SN relic neutrino for various cosmological models. All lines represent the differential number flux of $\bar{\nu}_e$s. The solid lines show the SN relic neutrino spectrum for a low-density, flat universe with $\Omega_0 = 0.2, \lambda_0 = 0.8$, and three different values of the Hubble constant; $h = H_0/(100\ \mathrm{km\ s^{-1}Mpc^{-1}}) = 0.5$(bottom line), $h = 0.8$(middle line)(this is their "standard model"), and $h = 1.0$(top line). The dashed line shows the SN relic neutrino spectrum for a low-density, open universe with $\Omega_0 = 0.2, \lambda_0 = 0.0$, and $h = 0.8$, and the dot-dashed line for an Einstein-de Sitter universe with $\Omega_0 = 1.0, \lambda_0 = 0.0$, and $h = 0.5$. For an illustrative purpose of comparison, the SN relic neutrino spectrum based on a model with the constant supernova rate is also shown by the dotted line, for which the constant supernova rate is normalized in such a way that the total (energy-integrated) SN relic neutrino is the same with that for the model with $\Omega_0 = 0.2, \lambda_0 = 0.8$, and $h = 0.8$ (solid, middle line). This figure is extracted from [8].

where the relation $n_G(t) = n_G(t_0)(1+z)^3$, which is the expansion effect, is used. Using (2.11), we now get the differential number flux of the SN relic neutrinos,

$$\frac{dF_R(E)}{dE} = \frac{c n_G(t_0)}{H_0} \int_0^{z_{max}} R_{\mathrm{SN}}(t'(z)) \frac{dN_\nu[E(1+z)]}{dE} \frac{dz}{\sqrt{(1+z)^2(\Omega_0 z + 1) - \lambda_0(z^2+2z)}}. \quad (2.17)$$

The difference of the expected flux among researchers is mainly come from the uncertainty of $R_{SN}(t)$.

Figure 2.6 shows the flux calculated by T. Totani, K. Sato, and Y. Yoshii [8]. Their "standard model" is used for the analysis of the SN relic neutrinos in this thesis, and their total flux is $44\ \mathrm{cm^{-2}sec^{-1}}$.

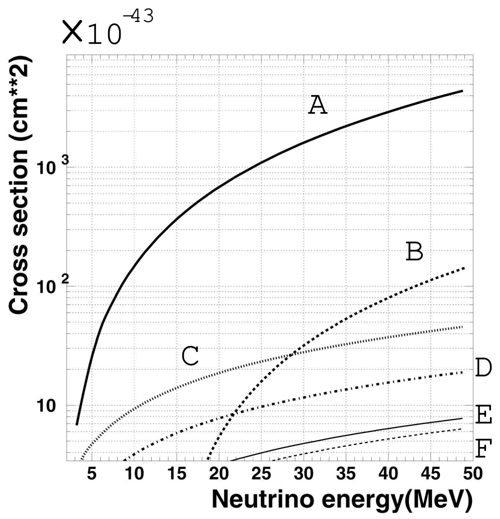

Figure 2.7: The cross sections for various neutrino reactions in water; A: $2\times(\bar{\nu_e}+p\rightarrow e^{+}+n)$, B: $\nu_e+{}^{16}O\rightarrow e^{-}+{}^{16}F$, C: $10\times(\nu_e+e^{-}\rightarrow\nu_e+e^{-})$, D: $10\times(\bar{\nu_e}+e^{-}\rightarrow\bar{\nu_e}+e^{-})$, E: $10\times(\nu_x+e^{-}\rightarrow\nu_x+e^{-})$, F: $10\times(\bar{\nu_x}+e^{-}\rightarrow\bar{\nu_x}+e^{-})$, where ν_x is ν_μ or ν_τ. For the reactions related to free protons or electrons, the cross sections are multiplied by 2 or 10, respectively.

2.8 Neutrino interactions with water

Super-Kamiokande is a water Cherenkov detector, which detects Cherenkov light emitted from a charged particle generated by the neutrino interaction in water. The SN relic neutrinos from the past supernovae comprise all species of neutrinos, $\overset{(-)}{\nu_e}, \overset{(-)}{\nu_\mu}, \overset{(-)}{\nu_\tau}$, and the energy is less than the muon mass (106 MeV/c^2). Reactions in water (H_2O) are

$$\begin{aligned}
\bar{\nu_e}+p &\rightarrow e^{+}+n && \text{(CC)} \quad (2.18)\\
\nu_e+e^{-} &\rightarrow \nu_e+e^{-} && \text{(CC,NC)} \quad (2.19)\\
\bar{\nu_e}+e^{-} &\rightarrow \bar{\nu_e}+e^{-} && \text{(CC,NC)} \quad (2.20)\\
\nu_x+e^{-} &\rightarrow \nu_x+e^{-} && \text{(NC)} \quad (2.21)\\
\nu_e+{}^{16}O &\rightarrow e^{-}+{}^{16}F && \text{(CC)} \quad (2.22)\\
\bar{\nu_e}+{}^{16}O &\rightarrow e^{+}+{}^{16}N && \text{(CC)} \quad (2.23)
\end{aligned}$$

where

$$\nu_x=\nu_\mu,\nu_\tau,\bar{\nu_\mu},\bar{\nu_\tau}. \quad (2.24)$$

The cross sections above are given in [23] and [24]. Figure 2.7 and 2.8 show cross sections for each reactions.

At the energy less than 50 MeV, the cross section of the interaction

$$\bar{\nu_e}+p\rightarrow e^{+}+n \quad (2.25)$$

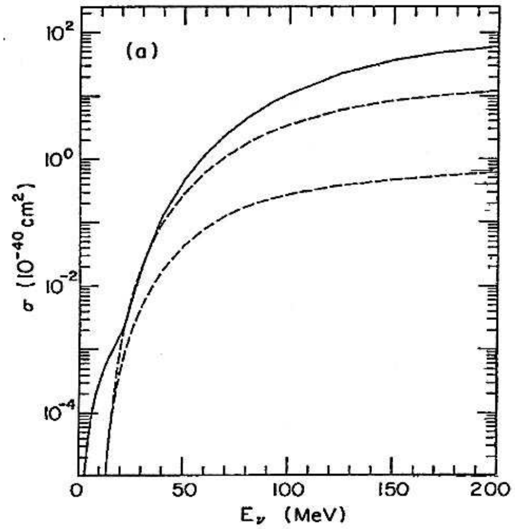

Figure 2.8: The cross sections of (anti-)electron neutrino with ^{16}O, extracted from [24]. The solid line shows the total cross section of the reaction $\nu_e + {}^{16}O \to e^- + {}^{16}F$, the upper dashed line shows that of the reaction $\bar{\nu_e} + {}^{16}O \to e^+ + {}^{16}N$.

is much larger than those of the other reactions, then we consider only this reaction. The total cross section of the reaction (2.25) is given by[17]

$$\sigma = 9.77 \times 10^{-44} E_e p_e \mathrm{cm}^2, \tag{2.26}$$

where

$$E_e = E_\nu - \Delta M;\ \Delta M = M_n - M_p = 1.3\mathrm{MeV} \tag{2.27}$$
$$p_e^2 = E_e^2 - m_e^2. \tag{2.28}$$

Thus, the energy of ν_e is obtained by measuring the energy of emitted positron, using the relation, $E_\nu = E_e + 1.3$MeV.

More precisely, the cross section of the reaction (2.25) is given as follows [25, 26]. The Lorentz-invariant amplitude ($\mathcal{M}$) of this reaction is

$$\mathcal{M} = \frac{G_F}{\sqrt{2}} < e^+(p_e)|j^{+\lambda}|\bar{\nu_e}(p_\nu) >< n(p_n)|J_\lambda^-|p(p_p) >, \tag{2.29}$$

$$< e^+(p_e)|j^{+\lambda}|\bar{\nu_e}(p_\nu) >= \bar{v}(p_e)\gamma^\lambda(1-\gamma_5)v(p_\nu), \tag{2.30}$$

$$< n(p_n)|J_\lambda^-|p(p_p) >= \cos\theta_c \bar{u}(p_n)\Gamma_\lambda u(p_p), \tag{2.31}$$

$$\Gamma_\lambda = \gamma_\lambda F_V^1(q^2) + \frac{i\sigma_{\lambda\nu}q^\nu \xi F_V^2(q^2)}{2M} + \gamma_\lambda\gamma_5 F_A(q^2), \tag{2.32}$$

where G_F is the Fermi constant, $\cos\theta_c$ is the Cabibbo angle, $M = (M_p + M_n)/2$ is the nucleon mass, $\xi \equiv \mu_p - \mu_n = 3.71$ (μ = anomalous magnetic moment) and F_V^1,F_V^2 and F_A are the vector and axial vector form factors expressed as:

$$F_V^1(q^2) = \left(1 - \frac{q^2}{4M^2}\right)^{-1}\left[G_E^V(q^2) - \frac{q^2}{4M^2}G_M^V(q^2)\right], \tag{2.33}$$

$$\xi F_V^2(q^2) = \left(1 - \frac{q^2}{4M^2}\right)^{-1}\left[G_M^V(q^2) - G_E^V(q^2)\right], \tag{2.34}$$

$$F_A(q^2) = \frac{-1.23}{\left(1 - \frac{q^2}{M_A^2}\right)^2}, \tag{2.35}$$

$$G_E^V(q^2) = \frac{1}{\left(1 - \frac{q^2}{M_V^2}\right)^2}, \quad G_M^V(q^2) = \frac{1+\xi}{\left(1 - \frac{q^2}{M_V^2}\right)^2}. \tag{2.36}$$

M_V and M_A are the vector and axial-vector masses and are taken to be 0.84GeV and 0.01GeV, respectively, according to Ref [27].

The cross section for this reaction is

$$\frac{d\sigma}{dt} = \frac{|\mathcal{M}|^2}{\pi(2M_pE_\nu)^2} \tag{2.37}$$

$$= \frac{M^2G^2\cos^2\theta_c}{8\pi E_\nu}\left[A(q^2) + B(q^2)\frac{(s-u)}{M^2} + \frac{C(q^2)\left((s-u)^2 - 4M^2(M_n - M_p)^2\right)}{M^4}\right] \tag{2.38}$$

where

$$A(q^2) = \frac{(m_e^2 - q^2)}{4M^2}\left[\left(4 - \frac{q^2}{M^2}\right)\left(F_A(q^2)\right)^2 - \left(4 + \frac{q^2}{M^2}\right)\left(F_V^1(q^2)\right)^2\right. \tag{2.39}$$

$$-\frac{q^2}{M^2}\left(\xi F_V^2(q^2)\right)^2\left(1 + \frac{q^2}{4M^2}\right) - \frac{4q^2F_V^1(q^2)\xi F_V^2(q^2)}{M^2} \tag{2.40}$$

$$\left.-\frac{m_e^2}{M^2}\left(\left(F_V^1(q^2) + \xi F_V^2(q^2)\right)^2 + \left(F_A(q^2)\right)^2\right)\right], \tag{2.41}$$

$$B(q^2) = -\frac{q^2}{M^2}F_A(q^2)\left(F_V^1(q^2) + \xi F_V^2(q^2)\right), \tag{2.42}$$

$$C(q^2) = \frac{1}{4}\left(\left(F_A(q^2)\right)^2 + \left(F_V^1(q^2)\right)^2 - \frac{q^2}{4M^2}\left(\xi F_V^2(q^2)\right)^2\right), \tag{2.43}$$

and where s, t and u are the Mandelstam variables, which are written in the laboratory frame:

$$s = (p_\nu + p_p)^2 = M_p^2 + 2M_pE_\nu, \tag{2.44}$$

$$t = (p_\nu - p_e)^2 = M_n^2 - M_p^2 - 2M_p(E_\nu - E_e) = q^2, \tag{2.45}$$

$$u = (p_\nu - p_n)^2 = M_p^2 + m_e^2 - 2M_pE_e. \tag{2.46}$$

Integrating $\frac{d\sigma}{dt}$ by t, the total cross section σ_{tot} is given.

2.9 Backgrounds

To search for the SN relic neutrinos, the reduction of the background and their estimation of the number of events are important. In this section the backgrounds for the SN relic neutrinos are described.

2.9.1 Atmospheric neutrinos

Cosmic ray is the extraterrestrial radiation from above the atmosphere of the Earth. Cosmic rays before striking into atmosphere are called *primary cosmic rays*. The ingredients of primary cosmic rays are as follows: $\sim$ 85% protons, $\sim$ 12% He nuclei, $\sim$ 1% heavier nuclei, and $\sim$ 2% electrons. After striking into atmosphere, primary cosmic rays interact with air nuclei (nitrogen and oxygen) and produce nucleonic cascade (air shower), making *secondary cosmic rays*. Figure 2.9 shows the development of a nucleonic cascade in the atmosphere. Secondary mesons decay and give rise to *atmospheric neutrinos*, which are composed of $\overset{(-)}{\nu_e}, \overset{(-)}{\nu_\mu}$. They originate mainly from the following decay chains:

$$
\begin{array}{llll}
\pi^+ \to \mu^+\nu_\mu, & \mu^+ \to e^+\nu_e\,\bar{\nu}_\mu; & & \\
\pi^- \to \mu^-\,\bar{\nu}_\mu, & \mu^- \to e^-\,\bar{\nu}_e\,\nu_\mu; & & \\
\mathrm{K}^+ \to \mu^+\nu_\mu, & \mu^+ \to e^+\nu_e\,\bar{\nu}_\mu; & & \\
\mathrm{K}^- \to \mu^-\,\bar{\nu}_\mu, & \mu^- \to e^-\,\bar{\nu}_e\,\nu_\mu; & & \\
\mathrm{K}^0_L \to \pi^-\mu^+\nu_\mu, & \pi^- \to \mu^-\,\bar{\nu}_\mu, & \mu^- \to e^-\,\bar{\nu}_e\,\nu_\mu, & \mu^+ \to e^+\nu_e\,\bar{\nu}_\mu; \\
\mathrm{K}^0_L \to \pi^+\mu^-\,\bar{\nu}_\mu, & \pi^+ \to \mu^+\nu_\mu, & \mu^+ \to e^+\nu_e\,\bar{\nu}_\mu, & \mu^- \to e^-\,\bar{\nu}_e\,\nu_\mu.
\end{array}
$$

A Monte Carlo simulation is made to estimate the number of events from atmospheric neutrinos in the Super-Kamiokande. More detail on Monte Carlo simulation is given in Chapter 7.

The *neutrino oscillation* effect changes the amount of this background. This effect is observed and confirmed by Super-Kamiokande. Because the flavor eigenstates $(\nu_e, \nu_\mu, \nu_\tau)$ are the mixture of the mass eigenstates (ν_1, ν_2, ν_3), the neutrinos change their flavor when they propagate through the vacuum. The probability that the ν_μ changes to ν_τ when traveling a distance L(km) through the vacuum can be written as:

$$P(\nu_\mu \to \nu_\tau) = \sin^2 2\theta \sin^2\left(\frac{\pi L}{L_V}\right) \tag{2.47}$$

where

$$L_V = \frac{4\pi E_\nu}{\Delta m^2} = 2.48\frac{E_\nu(\mathrm{MeV})}{\Delta m^2(\mathrm{eV}^2)}(\mathrm{m}) \tag{2.48}$$

is the oscillation length, E_ν(MeV) is the neutrino energy, $\Delta m^2(\mathrm{eV}^2)$ is the squared difference of the neutrino mass eigenstates, and θ is the mixing angle between the flavor eigenstates. The probability of the other oscillation modes are considered small enough as suggested by

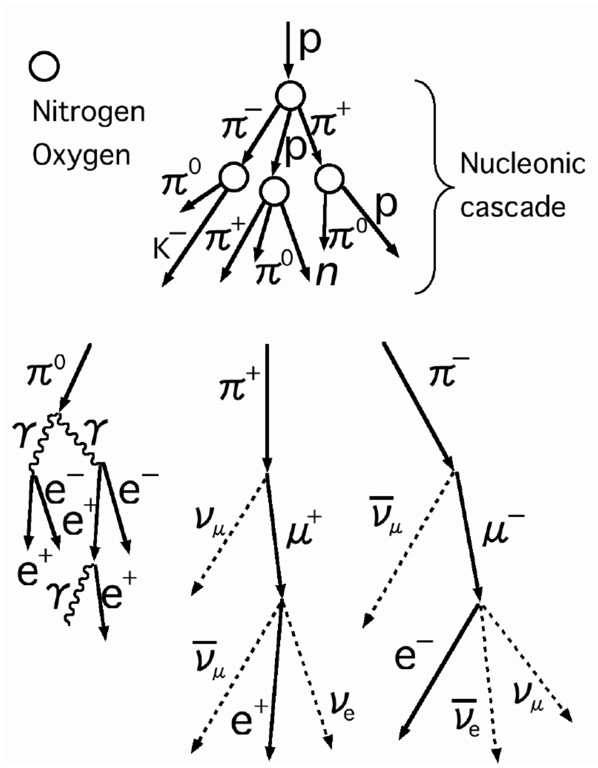

Figure 2.9: Production of atmospheric neutrinos

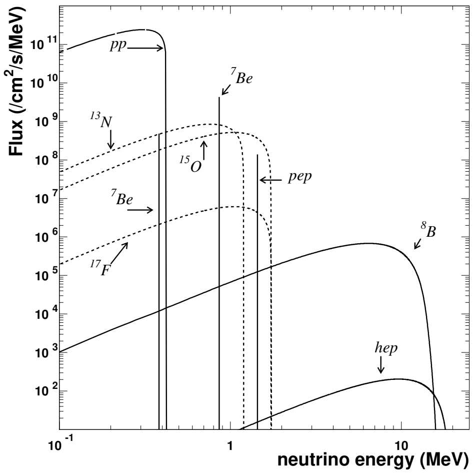

Figure 2.10: Energy spectrum of solar neutrinos

the atmospheric neutrino analysis. We adopt the oscillation parameters $\sin^2(2\theta) = 1$, $\Delta m^2 = 3 \times 10^{-3}\text{eV}^2$, which is the most plausible value obtained by [28].

2.9.2 Solar neutrinos

The sun is shining by the nuclear fusion reactions as described in [29]. On these reactions, the ν_es are emitted, which are called *solar neutrinos*. Figure 2.10 shows the energy spectrum of solar neutrinos.

The maximum energy of the solar neutrinos are 18.8 MeV of the *hep* neutrinos. When we search for the SN relic neutrino from the energy region below 20 MeV, we must reject such neutrino backgrounds. The direction of recoil electrons in the detector is strongly concentrated to the opposite direction of the Sun. Therefore, the solar neutrinos can be rejected, using the angle between the direction of the electron and the direction of the Sun.

2.9.3 Spallation background

High energy cosmic-ray muons striking into the detector often cause the following reaction, which is called *spallation*:

$$\mu +^{16} \text{O} \rightarrow \mu + \text{X} \tag{2.49}$$

where X is radioactive elements. The candidate elements of the spallation products are listed in table 2.1. β-rays and γ-rays emitted from these radioactive elements become background for neutrino observation. As for the solar neutrino observation, they are not so serious background, because the directions of β-rays and γ-ray are distribute uniformly, on the contrary, those of the recoil electrons scattered by solar neutrinos are concentrated to the opposite direction of the Sun. On the other hand, for the SN relic neutrinos, they are an intrinsic background, because they are diffuse neutrinos. To avoid this background, we search for the SN relic neutrinos in the energy range above 20 MeV. As shown in Table 2.1, around 20 MeV there are two nuclei for the background: β and $\beta + \gamma$ emitted from ${}^{11}_{3}\mathrm{Li}$ and ${}^{14}_{5}\mathrm{B}$, respectively, however because their lifetimes are short, they can be rejected. The reduction of these backgrounds are described in Chapter 6 in detail.

Isotope	$\tau_{1/2}$(sec)	Decay mode	Kinetic Energy(MeV)
$^{8}_{2}$He	0.122	β^-	10.66+0.99(γ)
		β^-+n	(11%)
$^{8}_{3}$Li	0.84	β^-	12.5∼13.0
$^{8}_{5}$B	0.77	β^+	13.73
$^{9}_{3}$Li	0.178	β^-	13.5(75%)
			11.0+2.5(γ)
		β^-+n	∼ 10(35%)
$^{9}_{6}$C	0.127	β^++p	3∼13
$^{11}_{3}$Li	0.0085	β^-	20.77(31%)
		β^-+n	∼16(61%)
$^{11}_{4}$Be	13.8	β^-	11.48(61%)
			9.32+2.1(γ)(29%)
$^{12}_{4}$Be	0.0114	β^-	11.66
$^{12}_{5}$B	0.0204	β^-	13.37
$^{12}_{7}$N	0.0110	β^-	16.38
$^{13}_{5}$B	0.0173	β^-	13.42
$^{13}_{8}$O	0.0090	β^-	8∼14
$^{14}_{5}$B	0.0161	β^-	14.07+6.09(γ)
$^{15}_{6}$C	2.449	β^-	9.82(32%)
			4.51+5.30(γ)
$^{16}_{6}$C	0.7478	β^-	∼4
$^{16}_{7}$N	7.134	β^-	10.44(26%)
			4.27+6.13(γ)(68%)

Table 2.1: Candidate of spallation products.

Chapter 3

Super-Kamiokande detector

The Super-Kamiokande[1] detector is a water Cherenkov detector filled with 50 kt water, located at the Kamioka Observatory of Institute for Cosmic Ray Research, University of Tokyo, in the Kamioka mine of Gifu prefecture, Japan. The center of the detector is at $36°25'33''$ N, $137°18'37''$ E, 371.8 m above the sea level. It is placed at 1000 meters (2700 meters-water-equivalent) below the peak of Mt. Ikenoyama, to reduce cosmic-ray muons background rate ($\sim$2Hz).

This experiment has started on April 1 1996 and the detector has operated stably to search for nucleon decays which are predicted by Grand Unified Theories (GUTs) and to study neutrinos such as atmospheric, solar and supernova neutrinos. In this chapter the details of this detector are explained.

3.1 Method

The Super-Kamiokande detector is a ring-imaging water Cherenkov detector which detects Cherenkov light emitted by charged particles traversing in water. A charged particle emits Cherenkov light when the velocity (v) exceeds the velocity of light in a medium (c/n), where n is the refractive index of the medium. Since that of pure water is about 1.33, the threshold momenta for the Cherenkov radiation are 0.58, 120, 158, and 1060 MeV/c for electrons, muons, pions, and protons, respectively.

This Cherenkov light is emitted in the forward direction of the traveling particle with an opening angle θ as:

$$\cos\theta = \frac{1}{n\beta}, \tag{3.1}$$

where $\beta \equiv v/c$. For example, θ is about 42^o in water when β=1.

[1] This is abbreviation of Kamioka neutrino detection experiment or Kamioka nucleon decay experiment

The number of photons emitted per unit path length per unit wavelength λ is expressed as:

$$\frac{d^2N}{dxd\lambda} = 2\pi\alpha\left(1 - \frac{1}{n^2\beta^2}\right)\frac{1}{\lambda^2}, \tag{3.2}$$

where $\alpha = 1/137$ is the fine structure constant and x is the path length of a charged particle. The number of Cherenkov photons emitted in the wavelength region 300nm $\sim$ 600nm, which is the sensitive region for photomultipliers (PMTs), is about 340 per cm in water.

Cherenkov light becomes a ring-like image and can be detected by PMTs on the wall (Figure 3.1).

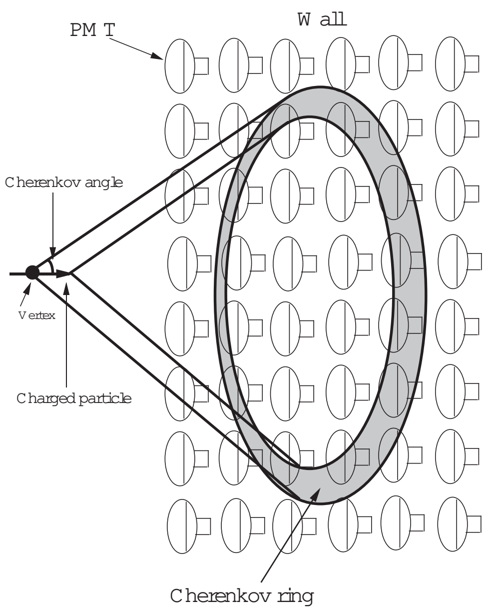

Figure 3.1: Schematic drawing of the method in detecting Cherenkov ring

3.2 Detector

The Super-Kamiokande detector is a cylindrical water tank with the height of 41.4 meters, the diameter of 39.3 meters and 50,000m^3 in volume. Figure 3.2 shows a view of the detector. The detector is optically separated into the inner detector (ID) and the outer detector (OD) by a pair of opaque sheets which enclose a dead region of $\sim$ 55cm in thickness as shown in Figure 3.3.

The inner detector with 32 kt of water is viewed by 11,146 PMTs of 20-inch diameter, facing inward to detect Cherenkov light produced within the ID. The outer detector, which completely surrounds ID with a layer of water of 2.6 - 2.75 m thick, has 1885 PMTs of 8-inch diameter used to veto entering events and to tag exiting events. We define the coordinates as shown in Figure 3.4 which is compared to geographical directions.

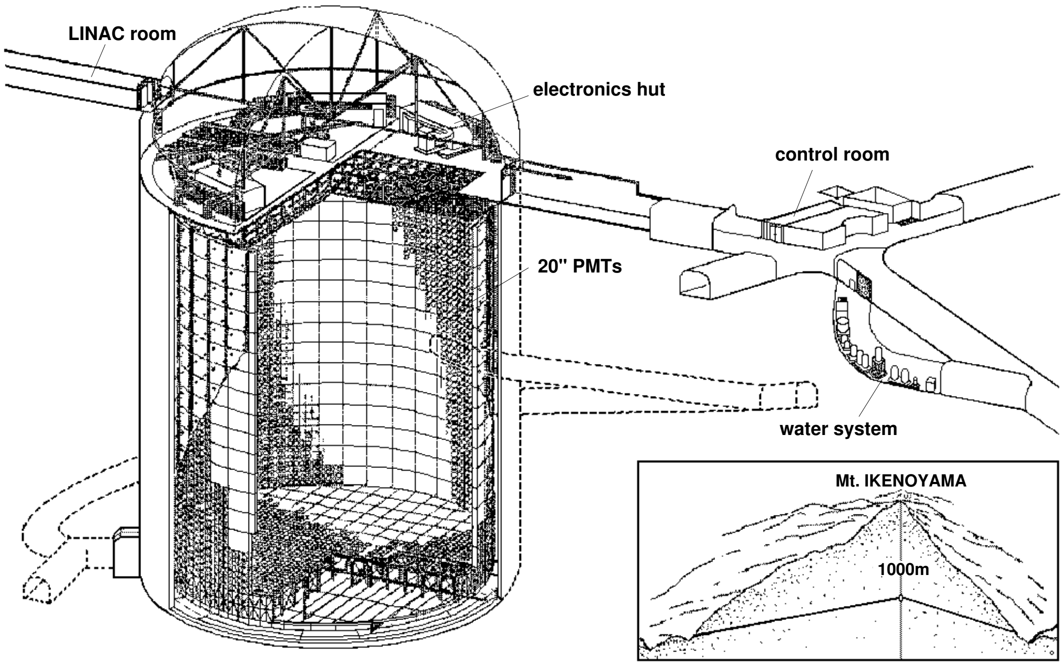

Figure 3.2: A schematic view of the Super-Kamiokande detector

3.3 Photomultiplier tube

The photomultiplier tubes (PMTs) used in the inner part of Super-Kamiokande are 20-inch diameter PMTs developed by Hamamatsu Photonics K.K. in cooperation with members of Kamiokande.The PMTs used in Super-Kamiokande were further improved over those used in Kamiokande to obtain higher timing and energy resolution.A schematic view of 20-inch PMT is shown in Figure 3.5. Table 3.1 shows the characteristics of the 20-inch PMT. The photocathode is made of bialkali (Sb-K-Cs) that matches the wave length of Cherenkov light. The quantum efficiency (Q.E.) is shown in Figure 3.6. A Venetian-blind type dynode is used for this PMT because of its large photosensitive area. However, this large photosensitive area makes the transit time longer (about 100nsec at 1 photo electron (p.e.) light level) and transit time spread becomes worse. This type also has a smaller collection efficiency for secondary electrons compared to other types. The bleeder-chain was optimized in order to achieve good timing response and collection efficiency. As the result of this optimization, an 11-stage voltage divider (with the ratios of voltage division 8:3:1...:1) was used, and three types of focusing mesh-plates

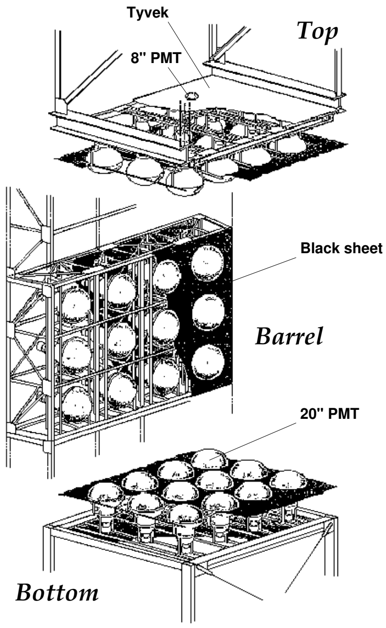

Figure 3.3: The structure of the frame for ID and OD PMTs.

between the cathode and the first dynode were adopted. The average value of the collection efficiency is more than 70%. The one photo electron peak can be seen clearly as shown in Figure 3.7. The transit time spread is about 2.2nsec. It is important for the analysis of solar neutrino data to have the ability to see 1 p.e. and good timing resolution, because the number of photons arriving at the PMT is generally one and the timing resolution affects the vertex reconstruction.

The residual geo-magnetic field is kept less than 100 mG in every position of the tank by using compensation coils.

The dark noise rate is stable and about 3.1 kHz after May of 1996. The number of accidental hits caused by the dark noise is estimated about 2 hits in any 50nsec time window. The dark

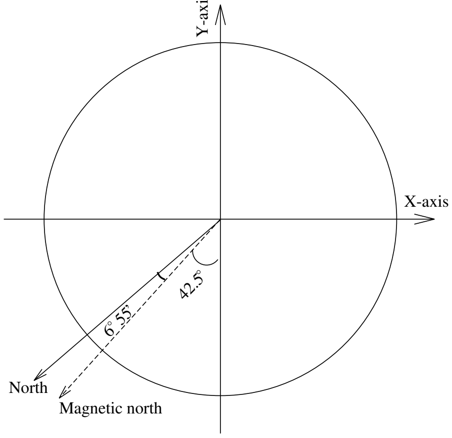

Figure 3.4: Coordinate of the Super-Kamiokande detector

Photocathode area	50cm (20 inch) in diameter
Photocathode material	Bialkali
Pressure tolerance	6 kg/cm^2 water proof
Quantum efficiency	20 % at $\lambda = 400$ nm
Gain	10^7 at ~ 2000 Volt
Dark current	200 nA at gain=10^7
Dark pulse rate	~ 3 kHz at gain=10^7
Transit time	90 nsec typical at gain=10^7
Transit time spread	2.8 nsec RMS at 1 p.e. equivalent signals

Table 3.1: The characteristics of the 20 inch PMT.

noise rate is considered in our Monte Carlo simulation program.

The PMTs used in the outer part are 8-inch Hamamatsu R1408 PMTs, each with a wave length shifter plate which is 60cm square to increase the light collection efficiency. Photons in the wave length range between 300 nm and 400nm are absorbed by the wave length shifter and about 55% of the photons isotropically re-emitted with a longer wave length.

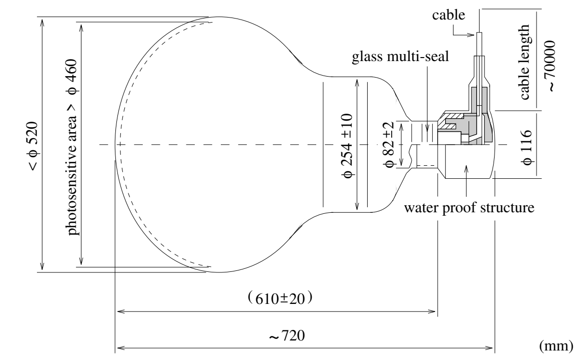

Figure 3.5: A schematic view of 50cm PMT used for ID.

3.4 Water purification system

To keep the light attenuation length long and to make water background free, water in the tank is circulated and purified continuously. This water purification system (Fig. 3.8) consists of several components:

1. 1 μm filter: to remove dust.

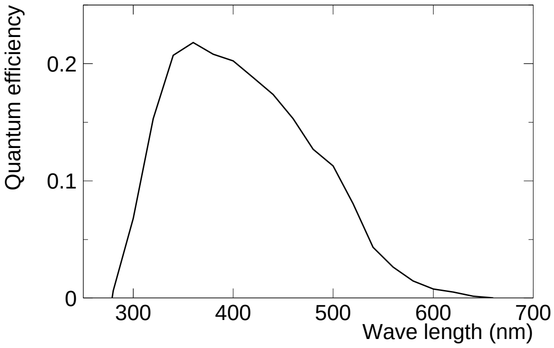

Figure 3.6: Quantum efficiency of PMT.

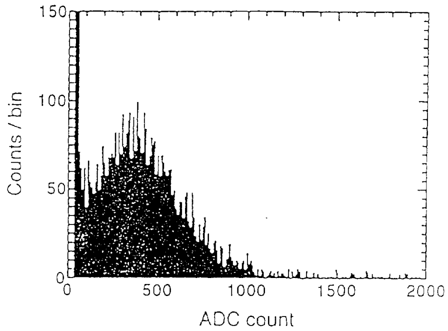

Figure 3.7: 1 p.e. distribution of the 50 cm PMT

2. Heat exchanger: to cool water temperature to 14^o to suppress bacteria growth.[2]

3. Ion exchanger: to remove metal ions such as Ra and Th in water.

4. Ultra-Violet sterilizer: to kill bacteria in water.

5. Vacuum degasifier: to remove gases such as oxygen and radon.

6. Cartridge polisher: to remove metal ions such as Ra and Th in water. This is high performance ion exchanger.

7. Ultra filter: to remove small dust down to the order of 10 nm.

8. Reverse osmosis: This is the high performance membrane which removes even organisms of the order of 100 molecular weight.

After this water purification, the level of radon contamination is reduced from 10^4Bq/m^3 (mine water) to $\sim$ 5mBq/m^3 and the light attenuation length is about 100m at a wavelength of 420nm which is suitable for a large water tank.

[2]Water temperature is heated by PMTs and pumps.

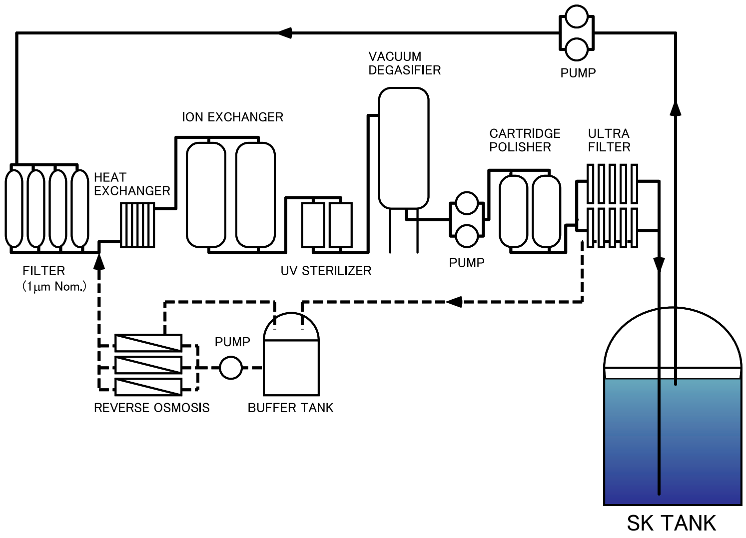

Figure 3.8: Water purification system at Super-Kamiokande.

3.5 Data acquisition system

3.5.1 Electronics

Figure 3.9 shows the data acquisition system for the inner detector. Signals from 11,146 PMTs are sent through 70 m long cables to a TKO (TRISTAN KEK Online) system, which is located on the tank inside the electronics huts. A TKO crate contains a GONG module[3], a SCH module[4], and 20 ATM modules[5].

The signals are first processed by ATM which record an amount of charge and timing of each PMT signal. In ATM, signals are divided into four. One goes to a discriminator and if the signal exceeds the threshold, HITSUM signals are sent to be used to generate the global trigger signal. HITSUM signal is a pulse with 200 nsec width and 15 mV/channel height. The other two (signal A and B) go through TAC (Time to Analog Converter) and QAC (Charge (Q) to Analog Converter) to measure time and charge information. If the global trigger is issued, the information in TAC/QAC is digitized and stored in 1024 word FIFO (First In/First Out) memory.

TAC and QAC has two channels A and B, into which signal A and B are taken, in order to take the data continuously without a dead time for successive events like a muon and a following decay electron. The forth is sent as PMTSUM. The ATM has ~ 450 pC dynamic range with a

[3]GO NoGo, which distributes control signals to its slave modules

[4]Super Controller Header, which is a bus-interface module between TKO and VME(Versa Module Europe)

[5]Analog Timing Module, which is ADC/TDC module, digitize analog signals from PMTs for timing and charge information and are controlled as slave modules by GONG

resolution of 0.2 pC in charge and $\sim$ 1300 nsec dynamic range with a resolution of 0.4 nsec in time. Each ATM can digitize 12 PMT signals.

There are 12 TKO crates in a electronics hut and 4 huts on the top of the Super-Kamiokande tank.

The digitized data in ATM are read out through SCH every 16 global triggers and stored in SMP (Super Memory Partner, VME specification). The memory in SMP is read by online slave workstations.

There is a completely independent data acquisition system for the outer detector. Figure 3.10 shows the outer data acquisition system at one of the electronics hut. It consists of 4 parts: 40 paddle cards where signal and high voltage lines are AC coupled , 10 QTCs (Charge to Timing Converters) modules where PMT signals are converted to logic pulses (ECL level), 5 TDCs (Time to Digital Converter) which are LeCroy 1877 TDC modules where signals are digitized in accuracy of 0.5 nsec, and one FSCC (FASTBUS Smart Crate Controller) where data are sent to online computer.

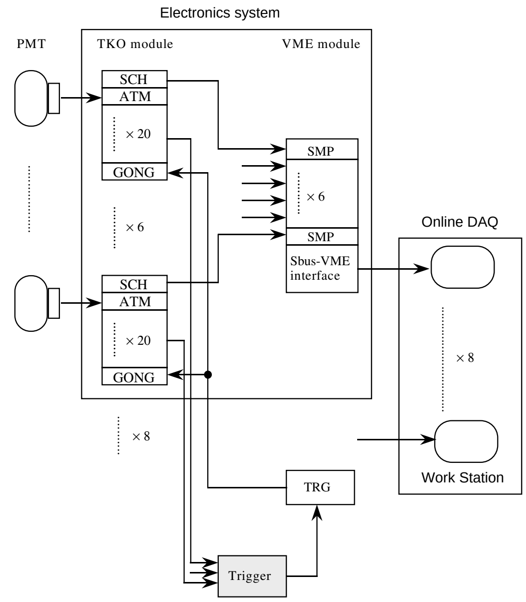

Figure 3.9: Data acquisition system for the inner detector.

3.5.2 Trigger system

The HITSUM signals from ATMs are summed up to generate grand HITSUM signal of the ID. Those from QTCs are also summed up separately to make grand HITSUM signal of the OD. These two signals are used to generate trigger signals for Super-Kamiokande detector. There are 3 triggers for the ID: High energy trigger (HE), Low energy trigger (LE) and Super

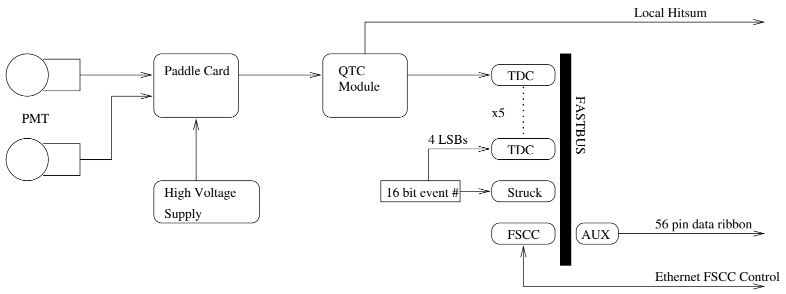

Figure 3.10: Data acquisition system for the outer detector.

Low energy trigger (SLE), requiring the discriminator threshold of -340mV, -320mV, and -260mV, respectively. HE trigger is a trigger used for quick identification of cosmic-ray muons, atmospheric neutrinos and proton decay candidates. LE and SLE triggers are for solar neutrino candidates. SLE threshold has being lowered gradually to get lower energy Solar neutrino events, recently it is set at -186mV. For LE, it select the events in energy range beginning at ∼5.7 MeV, while for SLE, energy range begins at lower than ∼4.6 MeV. The OD trigger is for identification of the cosmic-ray muons.

The global trigger is fed to the TRG module. This increments the 16 bit event number, distributes the event number signal and the global trigger signal to all GONGs, and records the time at which the global trigger was issued using an internal 50MHz 48 bit clock.

HE trigger is about 5∼6 Hz and LE trigger is about 10∼11 Hz and they are stable throughout the period. The trigger rate of OD trigger is ∼3 Hz.

3.5.3 Online and offline system

Data taking is operated in the units of *run*s by shift persons. The duration of 1 run is 24 hours basically, however, sometimes shorter because of hardware troubles, software troubles, or interruption of calibration. All events in some run are named (run number, event number), which is unique name of every event. For the first time, all PMT data of 1 event are gathered in a workstation, called *sukonh*, and named (run number, event number). These data are sent on to other workstations, called *sukonit*[n] ($n = 1, 2, \ldots$), where vertex positions of Super-Low-Energy triggered events are reconstructed and events are rejected when vertices are within 2 m distance from the ID wall. Further, these data are sent on to a workstation, called *sukrfm*, which changes the online format to an offline format (ZBS, Zebra Bank System), to make offline analysis more convenient. ZBS format is specially made for Super-Kamiokande experiment, from ZEBRA data structure (CERN library). We call this process *reformat*, and this ZBS format data *raw data* or *reformat data*. After reformat process is finished, the data are sent via optical fiber to the offline computer system which is outside of the mine. The transfer rate of reformatted data is about 100Mbyte/10minutes.

In offline computer system, the ADC and TDC counts of the ATM data are converted to the real charge (pC) and time (nsec), respectively, using the tables provided by various detector and electronics calibrations. This process is called *TQreal*. The size of data with real charge and time information is 27Gbyte/day. After TQreal, the reconstruction of events (vertex, direction, energy etc.) are carried out for solar neutrino, atmospheric neutrino, and upward-going muon events, independently. Data before the reconstruction of event are saved in MTL(Magnetic Tape Library) system until January 1998, and in PetaSite made by SONY since February 1998. Although these systems have large capacity of 12 Tbyte, and 100 Tbyte, respectively, the access speed to data is not so fast, then rereading of all data in this system is almost impossible because it takes about 1 year to reread 1 year data.

Chapter 4

Calibration

4.1 Xe calibration

The uniformity and stability of the gains of PMTs are necessary. The relative gains are calibrated by a scintillator ball with a Xe lamp as the light source. Figure 4.1 illustrates the setup of relative gain calibration. The relative gain of the i-th PMT is expressed as follows:

$$G_i = \alpha \cdot \frac{Q_i}{f(\theta)} \cdot r_i^2 \exp\left(-\frac{r_i}{L}\right) \tag{4.1}$$

where α is the normalization factor, Q_i is the measured charge of the i-th PMT, r_i is the distance from the light source to PMT, L is the light attenuation length and $f(\theta)$ is the relative photosensitive area as a function of PMT facing angle. The relative gain spread is about $\sim$7%. The overall gain for long time period is stable within 2% for 5 measurements in one year.

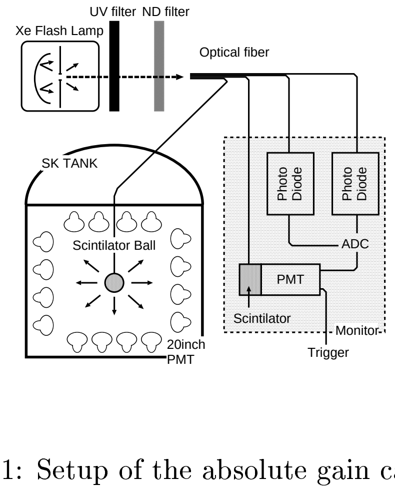

Figure 4.1: Setup of the absolute gain calibration.

4.2 Ni-Cf calibration

Figure 4.2 shows schematic view of Ni-Cf calibration source. Emitted neutrons from the spontaneous fissions of ^{252}Cf are decelerated by water to be thermal neutrinos. From neutron capture of Ni, γ-ray sources are produced and γ-rays with a maximum energy of 9.00MeV are emitted. Such γ-rays go out the container and scatters electrons by Compton scattering. Those electrons emit Cherenkov photons. In this case, signals on hit PMTs are at the 1p.e. level.

The single photoelectron distribution for a typical PMT is shown in Figure 4.2. The relation between pC and p.e. is determined as $1p.e.{=}$ 2.055pC.

The uniformity for single photo-electron efficiency is also investigated by this calibration. This revealed that the 375 PMTs produced in earlier period have higher 1p.e. efficiency. This fact is taken into account in the calculation of electron energy as described in equation 5.13.

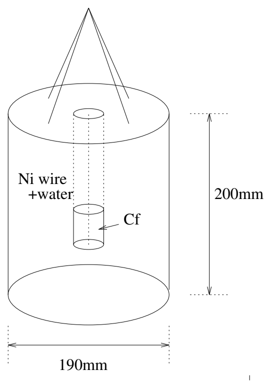

Figure 4.2: Schematic view of Ni calibration source

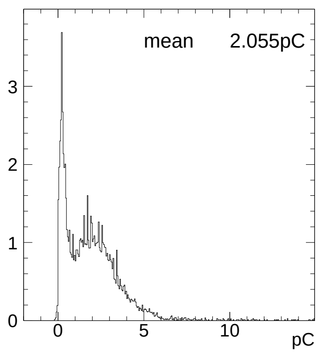

Figure 4.3: typical 1p.e. distribution.

4.3 Timing calibration

The timing calibration of PMTs are important for vertex position reconstruction. The time from each PMT varies by its timing response, its transit time and the pulse height. For this purpose, a light source of the diffuser ball is used. Figure 4.4 shows the setup of relative timing calibration.

Figure 4.5 shows the relation between the measured timing and the detected p.e. for a typical PMT. This is called TQ-map and we make the TQ-map for each channel. The typical timing resolution for a 1p.e. signal is 3nsec.

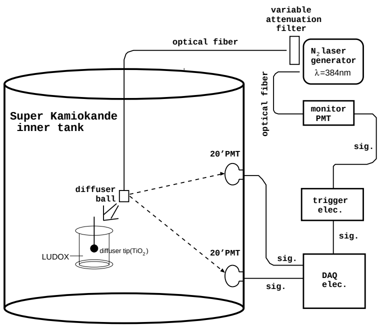

Figure 4.4: Setup of relative timing calibration.

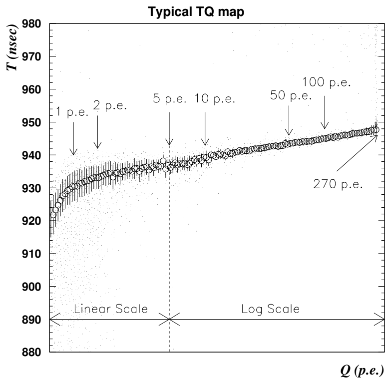

Figure 4.5: Typical TQ-map: circles and error bars show peak values and resolution.

4.4 Water transparency

The water transparency is important for energy determination.

This is measured by two independent methods: direct measurements by a dye laser and CCD camera, and indirect measurements by cosmic-ray muons.

4.4.1 Direct measurement of water transparency

Figure 4.6 shows the setup of water transparency measurement.

The water transparency was measured by the relation between the intensity at CCD camera I_{CCD} and 2-inch PMT I_{laser} which can be written as follows:

$$\frac{I_{CCD}}{I_{laser}} = const. \times \exp\left(-\frac{l_d}{L(\lambda)}\right) \times \frac{1}{l_d^2}, \tag{4.2}$$

where λ is the wavelength, $L(\lambda)$ is the attenuation length, l_d is the depth of the diffuser ball.

The result of this measurement is in Figure **??**

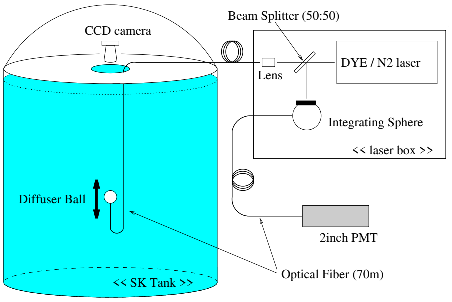

Figure 4.6: Setup of the water transparency measurement with dye laser and CCD camera.

4.4.2 Monitoring water transparency

The water transparency is monitored continuously using μ decay electron events.

Figure 4.7 shows schematic view of the method of water transparency calculation. For a decay electron event from a stopping muon, The hit PMTs, within a 50 nsec window after TOF subtraction and lying within a half opening angle of $32 \sim 52^o$ measured from its direction, are selected. They are divided into 36 azimuthal 10-degree bins. For the i-th bin effective charge on the sphere around the vertex with infinitesimal radius(R) is calculated by

$$\Delta Q_i = \sum_{j=1}^{N_i} q_j \exp(\frac{d_j}{\lambda}) \tag{4.3}$$

$$\cong \exp(\frac{r}{\lambda}) \sum_{j=1}^{k} q_j \tag{4.4}$$

$$= \exp(\frac{r}{\lambda}) q(r), \tag{4.5}$$

where $r \equiv \sum_{j=1}^{N_i} \frac{d_j}{N_i}$ is the mean distance and $q(r) \equiv \sum_{j=1}^{N_i} q_j$. Ideally ΔQ_i should satisfy the following relation,

$$\Delta Q_1 = \Delta Q_2 = \cdots = \Delta Q_{36} \equiv \Delta Q. \tag{4.6}$$

Every 7 days μ-decay electrons are collected and fitted as

$$\overline{q(r)} = \exp(-\frac{r}{\lambda})\overline{\Delta Q}. \tag{4.7}$$

Then,

$$\lambda = r \cdot \log(\overline{q(r)}/\overline{\Delta Q}), \tag{4.8}$$

where $\overline{q(r)}$ and $\overline{\Delta Q}$ are the average of $q(r)$ and ΔQ over 7 days, respectively.

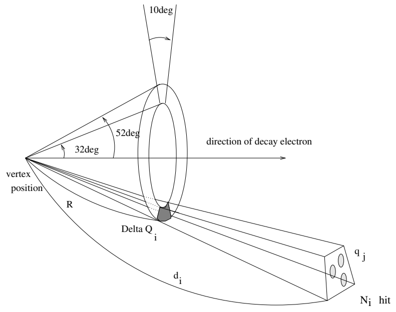

Figure 4.7: The method of calculating of the water transparency from a μ decay electron

4.5 LINAC calibration

A schematic view of LINAC system is shown in Figure 4.8. LINAC emits electrons with monochromatic energies of 5MeV $\sim$ 15MeV into the Super-Kamiokande tank directly. Energy, vertex and direction of electron are calibrated.

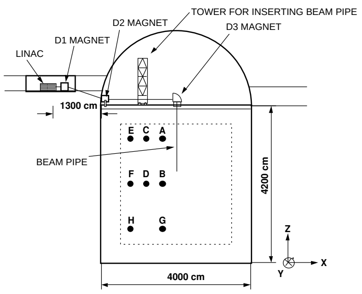

Figure 4.8: The schematic view of the LINAC calibration system.

Chapter 5

Event reconstruction

In this chapter event reconstruction for low energy events (Total charge $<$ 1000 p.e.) is described, where this total charge condition corresponds to $\lesssim$ 100MeV for the electron. At first the vertex of an event is reconstructed. After that, the event direction and energy can be reconstructed.

5.1 Vertex reconstruction

Figure 5.1 shows a display of a typical event, and Figure 5.2 shows the time distribution of the hit PMTs in the event of Figure 5.1.

The vertex where an event occur is reconstructed, using the timing information and the positions of the hit PMTs. For low energy events, the distance traversed by the electron is about $\lesssim$100cm, which can be regarded as a point, compared with the vertex resolution.

The method to select the signal PMTs are as follows:

1. A 200nsec timing window (WIN_{200}) which include the maximal number of hit PMTs is selected, where 200nsec is the time for the light to travel diagonally through the ID.

2. Within the WIN_{200}, 11 sub-timing windows (WIN_n), whose time widths are $\Delta t_n = 200n/11$ ($n = 1, 2, \cdots, 11$), are selected, where each sub-window includes the maximal number of hit PMTs, and $\mathrm{WIN}_n \subset \mathrm{WIN}_{n+1}$.

3. The significance S_n is calculated for each sub-window WIN_n as follows:

$$S_\mathrm{n} = \frac{N_\mathrm{sig}}{\sqrt{N_{noise}}}, \quad (5.1)$$

$$N_\mathrm{sig} = N_\mathrm{all} - N_\mathrm{noise}, \quad (5.2)$$

$$N_\mathrm{noise} = \Delta t_\mathrm{n} \times \frac{N_\mathrm{bef} + N_\mathrm{aft}}{\Delta t_\mathrm{bef} + \Delta t_\mathrm{aft}}, \quad (5.3)$$

where

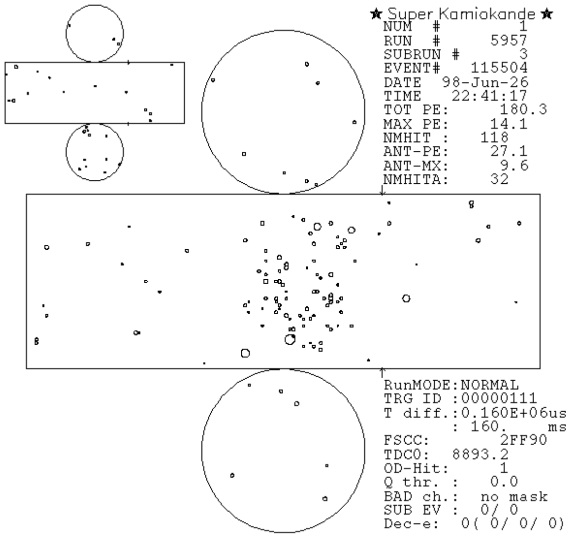

Figure 5.1: The view of a typical event: In this figure, the cylindrical ID tank is unfolded (large one) and also the OD (small one) are shown. Circles represent the position of hit PMTs. The radii of the circles reflect the magnitude of observed charges. A hazy Cherenkov ring can be seen.

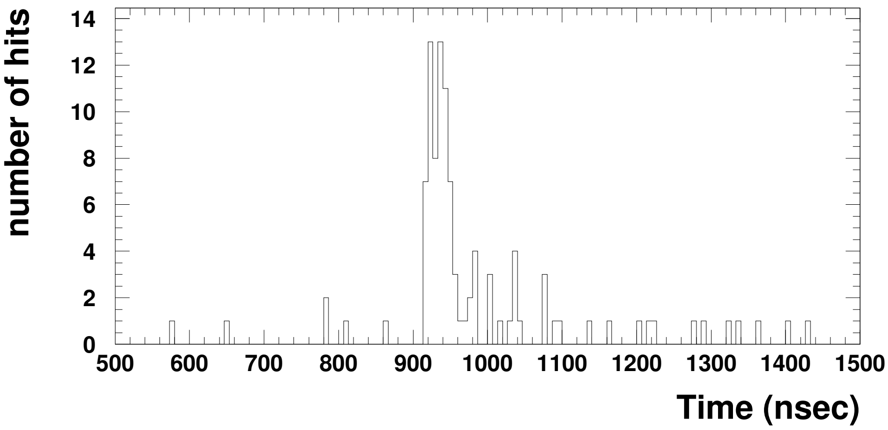

Figure 5.2: The time distribution of the hit PMTs in the event of figure 5.1. The horizontal axis is the absolute time, whose unit is nsec.

$N_{\rm sig}$:	the number of signal hit PMTs in WIN_n
$N_{\rm noise}$:	the number of noise hit PMTs in WIN_n
$N_{\rm all}$:	the number of all hit PMTs in WIN_n
Δt_n :	the time width of WIN_n
$N_{\rm bef}$:	the number of hit PMTs before WIN_n
$N_{\rm aft}$:	the number of hit PMTs after WIN_n
$\Delta t_{\rm bef}$:	the time width before WIN_n
$\Delta t_{\rm aft}$:	the time width after WIN_n

4. The widest sub-window which satisfies $S_n \geq 0.8 S_{\max} (S_{\max} = \max\{S_i | i = 1, 2, \cdots, n-1\})$ is selected.

The PMTs within the selected time window are used to reconstruct the vertex.

The vertex is determined as the point $(\mathbf{x})$ where the goodness $g_v(\mathbf{x})$ becomes maximum:

$$g_v(\mathbf{x}) = \frac{\displaystyle\sum_{i=1}^{N_v} \frac{1}{\sigma_i^2} \exp\left(-\frac{(T_{{\rm res},i}(\mathbf{x}))^2}{2\sigma_i^2} \right)}{\displaystyle\sum_{i=1}^{N_v} \frac{1}{\sigma_i^2}}, \tag{5.4}$$

where $T_{{\rm res},i}(\mathbf{x})$ is the residual time for the i-th hit PMT after subtraction of TOF[1], given by

$$\begin{aligned} T_{{\rm res},i}(\mathbf{x}) &= T_i - \frac{n}{c} d(\mathbf{x}, \mathbf{x}_i) - T_c, & (5.5) \\ &= T_{{\rm tof},i} - T_c & (5.6) \end{aligned}$$

where T_i, n, $d(\mathbf{x}, \mathbf{x}_i)$, and T_c are the time of the i-th hit PMT, the refraction index of water, the distance between the i-th hit PMT $(\mathbf{x}_i)$ and the vertex position $(\mathbf{x})$, and the peak in the $T_{{\rm tof},i}$ distribution, respectively. And N_v is the number of selected PMTs, σ_i is the time resolution of the i-th PMT. Each σ_i is inherently PMT-dependent, however, it is set to $<\sigma>= 5$nsec. A grid-search method is used to search for this maximum point.

5.2 Direction reconstruction

The vector $\mathbf{d}$ of the particle direction is determined that maximizes the logarithm of the likelihood function $(L(\mathbf{d}))$ given by:

$$\log(L(\mathbf{d})) = \sum_{i=1}^{N_{50}} \log\left(f(\cos\theta_{{\rm dir},i}(\mathbf{d}))\right) \frac{\cos\theta_i}{a(\cos\theta_i)}, \tag{5.7}$$

[1]Time Of Flight of light from the emitted point to the PMT.

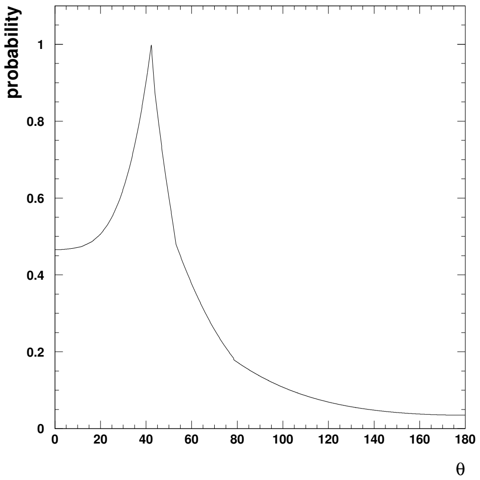

Figure 5.3: The unnormalized probability density function for Cherenkov photon directions with respect to initial electron direction for 10MeV/c electrons.

where N_{50} is the number of hit PMTs within the 50nsec window selected from $T_{\mathrm{tof},i}$ distribution and:

$$\cos\theta_{\mathrm{dir},i}(\mathbf{d}) = \frac{\mathbf{d}\cdot(\mathbf{x_i}-\mathbf{x_0})}{|\mathbf{d}||(\mathbf{x_i}-\mathbf{x_0})|} \tag{5.8}$$

is the angle between the direction $\mathbf{d}$ and the direction from the vertex point ($\mathbf{x}_0$) to the i-th PMT ($\mathbf{x}_i$). θ_i is the incident angle of Cherenkov photons to the i-th PMT. The function $f(\cos\theta)$ is a probability density function as shown in Figure 5.3. The function a$(\cos\theta)$ is the acceptance of the PMT as seen from the vertex position. As a function of the incident angle to the PMT, it is shown in Figure 5.4.

In order to get the direction which maximizes the likelihood function, a grid search method is employed. As the initial direction, the vector sum $\sum(\mathbf{x_i}-\mathbf{x_0})$ is used. The grid size is 20° in the first step, and is decreased down to 1.6° as the likelihood function is nearing its maximum.

5.3 Energy reconstruction

The total charge of the event is not a good indicator for low energy events, because most of the hit PMTs catch only a single photo-electron and charge resolution at the single photo-electron level of a 50cm-PMT is not good (~50%) enough.

Then we use the energy calculated from the number of hit PMTs within a 50nsec timing

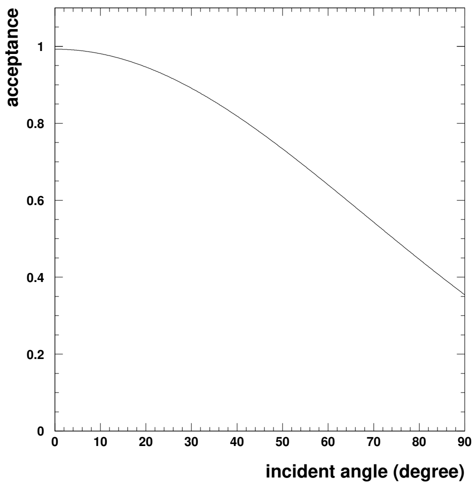

Figure 5.4: The acceptance function of the PMT.

window (N_{50}), and apply various corrections. The corrected number of hits, N_{eff}, is defined by:

$$N_{eff} = \sum_{i=1}^{N_{50}} \frac{N_{all}}{N_{alive}} (\alpha_i + \alpha_{tail} - \alpha_{dark}) S(\theta_i, \phi_i) e^{\frac{R(\mathbf{x}_0, \mathbf{x}_i)}{\lambda}} p_i. \tag{5.9}$$

N_{all}/N_{alive} is the correction factor for dead PMTs, where N_{all} is the total number of PMTs in the ID (11,146), and N_{alive} is the number of PMTs alive in the detector. α_i is the expected number of p.e. detected by the i-th hit PMT, which is estimated using the number of the hit PMTs neighboring the i-th PMT, given by:

$$\alpha_i = \begin{cases} \frac{\log(1/(1-\varepsilon_i))}{\varepsilon_i} & (\varepsilon_i < 1) \\ 3 & (\varepsilon_i = 1) \end{cases}, \tag{5.10}$$

where $\varepsilon_i = n_i/N_i$; n_i and N_i are the number of hit PMTs and the number of PMTs alive surrounding the i-th hit PMT (normally $N_i = 3 \times 3 = 9$).

α_{tail} is to recover the reflected Cherenkov photons which hit PMTs with a considerable time lag ($\leq$ 50nsec), given by:

$$\alpha_{tail} = \frac{N_{100} - N_{50}}{N_{50}}, \tag{5.11}$$

where N_{100} is the number of hit PMTs within the TOF subtracted 100nsec timing window.

α_{dark} is to subtract the dark noise of hit PMTs, given by

$$\alpha_{dark} = \frac{N_{alive} R_{dark} \times 100 \cdot 10^{-9}}{N_{50}}, \tag{5.12}$$

where R_{dark}(Hz) is the mean dark rate evaluated on a run-by-run basis.

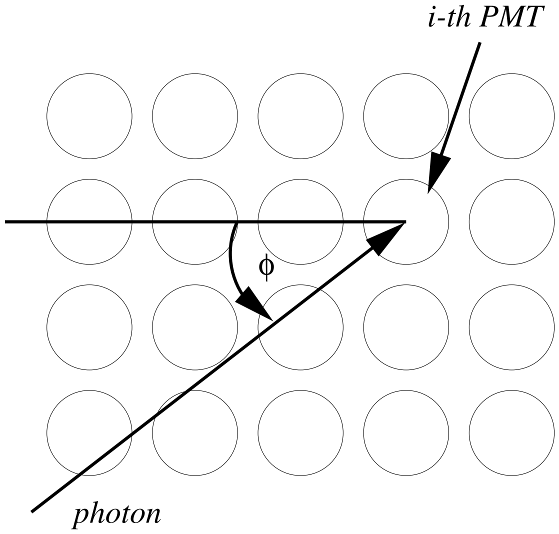

Figure 5.5: The arrangement of PMTs and the definition of the azimuthal angle ϕ.

$S(\theta_i, \phi_i)$ is the effective photo-cathode area viewed from the θ_i, ϕ_i direction, where θ_i is the incident angle to the i-th PMT and ϕ_i is the azimuthal angle. A ϕ dependence is caused by the arrangement of PMTs as shown in figure 5.5. The function $S(\theta, \phi)$ is shown in figure 5.6. $e^{\frac{R(\mathbf{x}_0, \mathbf{x}_i)}{\lambda}}$ is for compensation about the attenuation of Cherenkov light in water, where λ is the water transparency, which is measured using the Cherenkov light emitted from the decay electrons of stopping muons.

The last term p_i is the quantum efficiency correction factor. 375 PMTs were produced in a pre-series to the main PMTs. The quantum efficiency of these PMTs is found to be larger. The factor is given by:

$$p_i = \begin{cases} 0.833 & \text{(375 PMTs)} \\ 1.000 & \text{the other PMTs.} \end{cases} \tag{5.13}$$

5.4 Reconstruction of cosmic-ray muons

To reject spallation background, the fitting of the track of the cosmic ray muon is necessary. Reconstruction of the muon event proceeds in two steps. The first step is called *fast reconstruction*. The entrance position is obtained as the position of the PMT which is hit the earliest and has more than 2 neighboring hits within 5nsec. The exit position is defined as the center of gravity of the PMTs which detect more than 231p.e.,which is called *charge-saturated PMTs*. The muon track is the line connecting the entrance and the exit point.

If the condition below is satisfied, this reconstruction is regarded to be succeeded:

$L_{ent} > 300$cm and $L_{exit} < 300$cm,

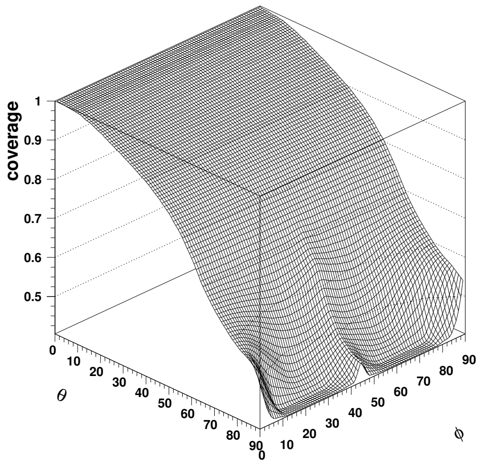

Figure 5.6: Effective photo-cathode area as a function of θ_i, ϕ_i direction.

where L_{ent} is the minimum distance between each charge-saturated PMT position and the entrance point, and L_{exit} is the maximum distance between each charge-saturated PMT position and the exit point.

If the first reconstruction fails, the second reconstruction is executed. When the number of the charge-saturated PMTs is large, the first reconstruction may fail. Therefore, events with a residual charge Q_{res}[2] greater than 25,000p.e. are always sent to the second reconstruction step.

In the second reconstruction, the entrance point is the same as the first reconstruction. The exit point is searched for so as to maximize the goodness g_μ defined by:

$$g_\mu = \frac{\sum_i \frac{1}{\sigma_i^2} \exp\left\{ -\frac{1}{2} \left(\frac{t_i - T}{1.5\sigma_i} \right)^2 \right\}}{\sum_i \frac{1}{\sigma_i^2}} \tag{5.15}$$

$$t_i = T_i(\mathbf{x}_i) - \frac{l_\mu(\mathbf{x}_{exit})}{c} - \frac{n\, l_{photon}(\mathbf{x}_{exit})}{c} \tag{5.16}$$

where $\mathbf{x}_{exit}$ is the exit point and T is the arrival time of the muon. $l_\mu(\mathbf{x}_{exit})$ and $l_{photon}(\mathbf{x}_{exit})$ are defined in figure 5.7.

If $L_{ent} > 300$cm, $L_{exit} < 300$cm and $g_\mu > 0.88$, this muon fit is regarded as successful. Events which do not satisfy this condition are regarded as unfitted.

[2] Q_{res} is defined by:

$$Q_{res} = Q_{total} - pL \tag{5.14}$$

where Q_{total} is the total photo-electrons observed in the event, L(cm) is the track length, p = 23p.e./cm is the average number of observed photo-electrons per unit track length for muons.

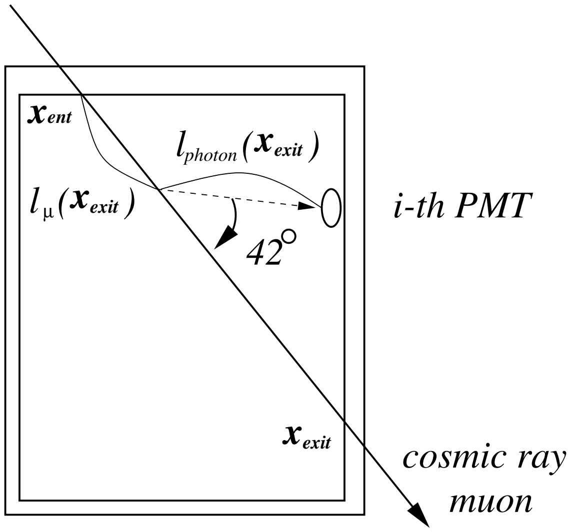

Figure 5.7: The definition of the variables used by the second muon reconstruction.

muon type	number of events	number of unfitted events
single muon	835	5
stopping muon	10	8
hard interaction	41	2
edge clipping	58	19
multiple muon	56	28
total	1000	62

Table 5.1: The fitting efficiency for the classified muon events.

The efficiency for this muon track reconstruction is shown in Table 5.1. Where the meaning of the muon types is as follows:

- single muon events : events which contain only a single muon track
- stopping muon events : muon events stopping in the ID
- hard interaction events : events with Q_{res} ≥25000p.e.
- edge clipping events : muons with track length less than 5m
- multiple muon events : events which contain more than or equal to 2 muon tracks

About 6% of the muon events are not fit.

Chapter 6

Reduction

6.1 Data Set

Super-Kamiokande has started taking data from April 1, 1996. Since purity of the tank water was not so good and Radon concentration in water was high in the first 2 months, we use the data after this period for solar neutrino or supernova neutrino analysis. In this thesis, data taken from May 31, 1996 to Oct 6, 2000, corresponding to the run number from 1742 to 9299 are used.

In this period, the operation time is assigned mainly for normal data taking and the other for the calibration of the SK detector. Among the normal runs, bad runs are rejected. The criterion of the bad run is described later in this Chapter. Finally, we obtain the total livetime of 1260 days.

To search for the SN relic neutrinos, the data made for solar neutrinos are useful, because the energy range of both are close; the SN relic neutrinos are $E_\nu \lesssim 50MeV$, solar neutrinos $E_\nu \lesssim 20MeV$. Hereafter the method of event reduction for the SN relic neutrinos are described. Most of the methods are the same as those for solar neutrinos, but some cuts are unnecessary and thus are omitted. Some cuts are specific cuts for the SN relic neutrino analysis.

6.2 Event Reduction

This section describes the data reduction in due order.

6.2.1 Total charge cut

Events whose ID total charge are $\geq$ 1000 p.e. are rejected. which corresponds to $\lesssim$ 130(MeV/c) for the electron or to $\lesssim$ 300(MeV/c) for the muon. This is to reject high-energy events, for example, cosmic-ray muon events (deposit energy $\sim$ 8 GeV), atmospheric neutrino events (deposit energy $\sim$ 1 GeV).

After this cut, reconstruction of events (vertex, direction, energy, etc.) are made, which is described in Chapter 5 in detail. Many parameters used in the following are calculated here.

After reconstruction of events, data are stored in hard disk in the *vector format*, which is made of structure of the C program language. So we can access and analyze these data easily and quickly. These data are used for the SN relic neutrino analysis in this thesis.

6.2.2 Bad run cut

The following sub-runs[1] are rejected.

- total run time of one sub-run $\leq$ 30sec.
- total live time of one run $\leq$ 5min.
- the rate of bad quality events (flasher, noise, etc.) is extremely high.

6.2.3 1st. reduction

Unfitted event cut

This cut reject events which have failed vertex reconstruction. There, the number of hit PMTs is too few to reconstruct a vertex position.

Fiducial volume cut

The volume where the distance from the nearest detector surface ($D_{\rm wall}$) is $\geq$ 200 cm is called *fiducial volume*. Events whose vertex positions are outside the fiducial volume are rejected. This is to reject events of radioactive rays (γ-ray or β-ray) which come from the detector wall or surrounding rock. The electrons produced by decay of the *invisible muons*[2] which penetrate into fiducial volume from the outside of the detector are also rejected by this cut, because invisible muons cannot travel more than $\sim 1m$ before its decay. This cut decreases the target volume for the neutrinos: 32ktons $\rightarrow$ 22.5ktons.

Time difference cut

The events whose time difference from the previous event $\leq 50\mu$sec are rejected. This cut is in order to eliminate decay electron events produced by cosmic ray stopping muon, after-pulse events, etc.

[1] The data of 1 run are divided into multiple files, which is called sub-run. Each sub-run is about 10 minutes.

[2] The word *invisible* means that it cannot be detected. That is, its momentum is less than the Cherenkov threshold, or Cherenkov light is too little to be triggered. In this case, this muon is a cosmic-ray muon itself, or the product of neutrino or muon reactions.

Genuine events related to the neutrino reaction, for example, decay electron from the muon which produced by ν_μ are also cut out here. Then after this cut, the first events of these correlated events can be not identify as the muon event easily. The recovery of this following events are described later in this Chapter. Dead time caused by this cut is 1.8×10^{-4}, which is negligible for the SN relic neutrino search.

Pedestal event cut

In data taking, pedestal values of ADCs on ATMs are taken every 30min. The events during this are incomplete, then abandoned.

Incomplete event cut

In rare occasion, there are online troubles caused by a breakdown or a bad behavior of the hardware. In this case, the data taken are incomplete. The online process can find these incomplete data and add a special flag event by event. The events whose flags denote that ID is off, OD off, or ATM data incomplete are rejected.

OD triggered event cut

Particles coming from the outside of the detector emit Cherenkov light and detected by the OD. The OD triggered events are rejected. And the events whose number of the hit PMTs in the OD > 20 are also rejected.

Noise event cut

The electronic noise sometimes happens. Sources of the noise are suspected to be PMT flashing, turning on-off of fluorescent lights, and so on. The feature of this kind of events is that noise hit channels have small charges. Then, a following variable is defined,

$$N/S = \frac{\text{number of hit channels } (|Q_{PMT}| < 0.5\text{p.e.})}{\text{total number of hit channels}}, \tag{6.1}$$

where $|Q_{PMT}|$ is the absolute charge value of a hit ATM channel. The events whose $N/S \geq 0.4$ are rejected.

Further, these noise hit channels are often clustered in one ATM board. Then the events which have the following values are rejected.

$$\text{ATMratio} \equiv \max\left(\frac{\text{number of hits in one ATM board}}{\text{number of channels in one ATM board}}\right) \geq 0.95 \ .$$

Bad goodness event cut

If a goodness g_v (see Equation 5.4) of an event is low, the reconstructed vertex position of the event is unreliable. Then the events whose goodness is < 0.4 are rejected.

External flasher cut

The events which satisfy the following conditions are rejected: goodness < 0.6 and $Dirks^3$ ≥ 0.25. This cut is for the specific flasher events.

Energy cut

The less the energy is, the more number of events exist in the data sample. we select the events whose energy is $\geq$ 6.5MeV.

6.2.4 Spallation cut

In order to reject spallation events, time and spatial correlation between the low energy events and preceding muons are used. The originating muons often deposit a large pulse height in the ID. Then the charge of the muon event is also taken into account. A *spallation likelihood*(L) is defined using these correlations.

Events with $L > 0.98$ (for reconstructed muon events) and $L > 0.92$ (for non-reconstructed muon events) are rejected as the spallation events. The dead time for the spallation cut is 20%.

6.2.5 2nd. reduction

Gringo cut

At the points around the reconstructed vertex, the goodnesses are calculated, If an event includes noise hit PMTs, such goodnesses distribute broad, otherwise narrow. Using this difference the noise events are rejected.

Patlik cut

On the β-decay of spallation products, some elements emit γ-rays as well as β-rays. In this case a Cherenkov ring pattern is disturbed by other rings. The pattern likelihood (*patlik*) is calculated, as compared with a Cherenkov ring pattern which is obtained by Monte Carlo simulation. The events whose *patlik* is ≤ -1.85 are rejected.

Clusfit cut

Using the relation of the distance and the time between the reconstructed vertex and the hit PMTs, noisy hit PMTs are removed. After removing these PMTs, the vertex is reconstructed, again. If the new vertex is outside of the fiducial volume, such an event is rejected.

[3] To test the direction, reconstructed by the method described in Chapter 5, of events *Dirks* is defined. If this value is large, this direction is not reliable.

6.2.6 Energy cut

The less the energy is, the more number of events exist in the data sample. we select the events whose energy is $\geq$ 14MeV.

6.2.7 Muon cut

The reductions described above are originally developed for the solar neutrino analysis, then tuned for the energy below 20MeV. For the SN relic neutrino analysis, such reductions are not enough. In fact there are many muon events remaining at this stage, (for example, see Figure 6.1 and 6.2). To reject muon events, further 2 types of muon cuts are developed.

Muon event followed by the decay electron

In water, 92.3% of muons decay to produce electrons and the rest are captured by an ^{16}O nucleus. So, lifetime in water is 2.08μsec, which is shorter than 2.20μsec in vacuum. Then when muons are produced by neutrino interactions within the tank, most of them are followed by decay electrons. In Super-Kamiokande, such muons and decay electrons are observed as 3 types of events as shown in Figure 6.3. In this figure, the horizontal (vertical) axis shows time (the number of hit PMTs). The pulse below shows the TDC gate. In *gate-in type*, a muon decays within the TDC gate, then the muon and electron signals are included in one event. In *sub-event type*, a muon decays after its TDC gate closing, then the two pulses of muon and electron are separated into two events[4]. In *bye-bye type*, a muon decays when its TDC gate is closing and the decay electron triggers opening the next TDC gate. Such decay electrons had not been detected efficiently. In 22 January, 1999, we installed the *after trigger*, a compulsive trigger opening another gate in 840 nsec after every HE trigger, since then, decay electrons of this type have been detected more efficiently.

At this stage of the reduction, sub-event type events have been rejected by time difference cut mentioned above. To investigate whether an event is followed by the sub-event or not, we must search for sub-events from the data file before the time difference cut is made. In most cases, the total charge of a sub-event is less than 1000 p.e., then it is enough for sub-events to be searched from the data after reconstruction. However, for example, if a neutrino reaction is followed by a multiple pion production, there are multiple muons, then multiple decay-electrons. Such an event may be followed by sub-events whose total charge is greater than 1000p.e. So, sub-events must be searched from so-called raw data. For this purpose, data format of events are converted to ZBS so as to be attached with sub-events. After attaching sub-events, muon events followed by decay-electrons are rejected.

[4]Sub-events are events occurring within 50μsec after the first event.

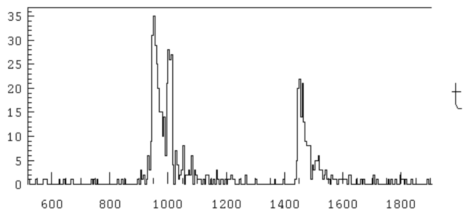

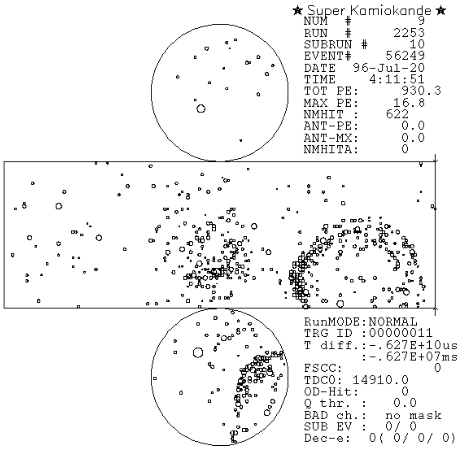

Horizontal (vertical) axis is the time in nsec (the number of hit PMTs). The first peak is caused by the Cherenkov light emitted from a muon, the second by that from a decay electron.

The right ring is a Cherenkov ring emitted from a muon and the left is that from a decay electron.

Figure 6.1: gate-in decay of a muon: the left is the time distribution and the right is the display image.

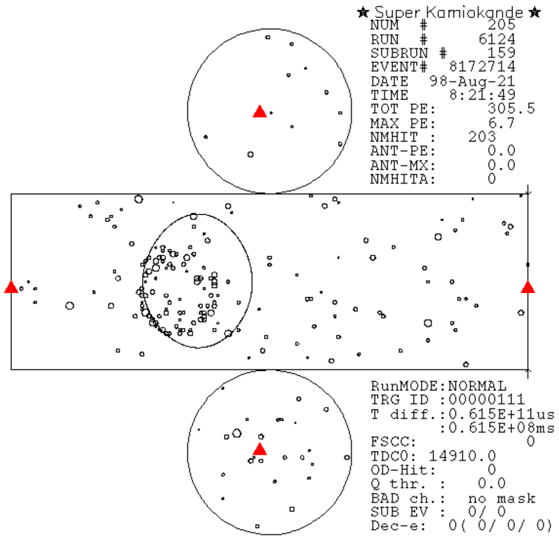

Figure 6.2: muon 1 ring

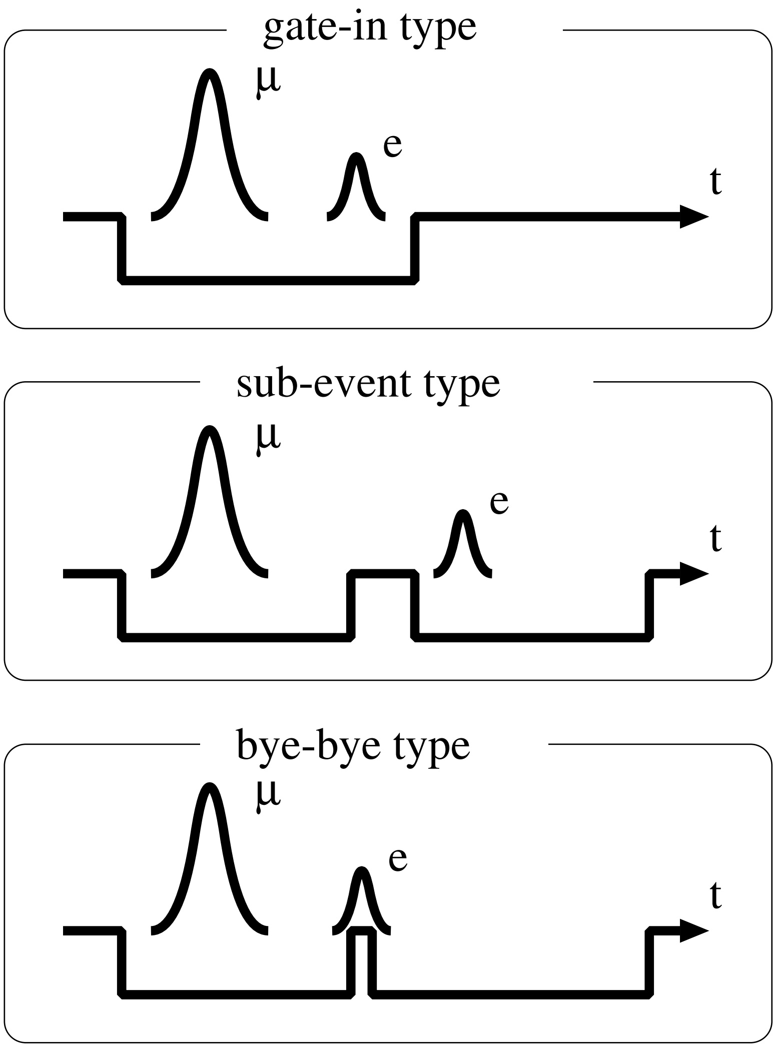

Figure 6.3: 3 types of muon decay events.

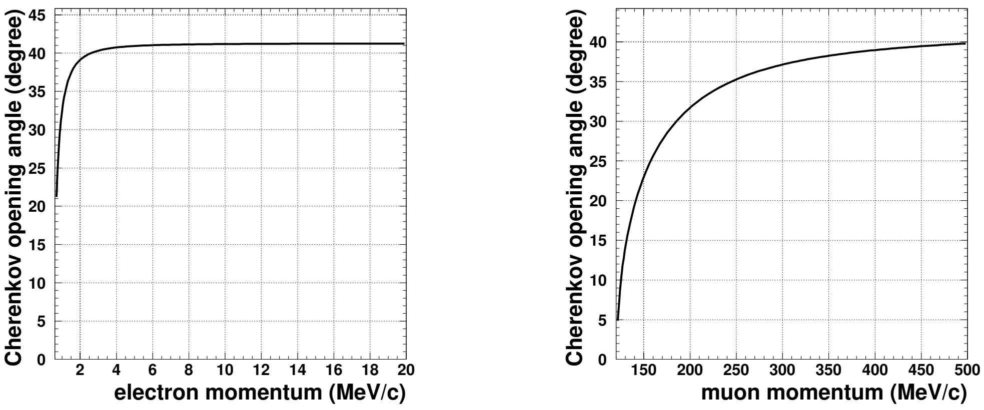

Figure 6.4: Cherenkov opening angle for electrons (left) and muons (right) vs. momentum.

Cherenkov angle distribution for muons

As mentioned above, 7.7% of muons are captured by ^{16}O nucleus, and are not followed by decay electrons. Then they cannot be rejected by the method above. Figure 6.2 shows a muon event. We can see PMTs which constitute one Cherenkov ring, and a solid line ring corresponding to an electron Cherenkov ring, which has 42 degree opening angle.

A muon whose fake energy is reconstructed as electron by the method 5 is $\lesssim$ 100 MeV has the momentum $\lesssim$ 300 MeV/c. Figures 6.4 shows Cherenkov angle (degree) as a function of the electron or the muon momentum. They show that we can separate electrons and muons by using the difference of Cherenkov opening angle.

The method is as follows:

1. Using the vertex reconstructed by the method described in Section 5.1, 50 nsec timing window is selected. It is determined to have the maximal number of hit PMTs in TOF subtracted time distribution.

2. The effective number of p.e. ($n_{\mathrm{eff}\,i}$) are calculated for each hit PMT as follows:

$$n_{\mathrm{eff}\,i} = \alpha_i S(\theta_i, \phi_i) e^{\frac{R(\mathbf{x}_0, \mathbf{x}_i)}{\lambda}} p_i \tag{6.2}$$

   where α_i, $S(\theta_i, \phi_i)$, $\frac{R(\mathbf{x}_0, \mathbf{x}_i)}{\lambda}$ and p_i are the same as described in Section 5.3.

3. The direction of particle ($\vec{d}$) is determined as the sum of the vector weighted by the effective number of p.e.:

$$\vec{d} = \sum_{i=1}^{N_{50}} n_{\mathrm{eff}\,i} \times \overrightarrow{(\mathrm{vertex})(\mathrm{hit\ PMT})}_i \tag{6.3}$$

where $\overrightarrow{(\text{vertex})(\text{hit PMT})}_i$, and N_{50} are the vector from the vertex to the i-th hit PMT, and the number of hit PMTs within a 50nsec timing window.

Figure 6.6 shows the effective number of p.e. distributions as a function of Cherenkov opening angle (θ), which is defined in Figure 6.5.A variable *ratioLR* is defined as follows.

$$\text{ratioLR} = \frac{[\text{effective p.e.}(0 \le \theta \le 40) - \text{effective p.e.}(40 < \theta \le 180)]}{\text{effective p.e.}(0 \le \theta \le 180)}. \tag{6.4}$$

We reject events with ratioLR > 0.

Figure 6.7 shows ratioLR distribution for electrons and muons made by Monte Carlo simulation. Figure 6.8 shows the same distribution for real events of 1260 day data sample.

6.2.8 Tight spallation cut

There are two candidates of spallation products. They emit radioactive particles that can be background for the SN relic neutrino search. They are ${}^{11}_{3}\text{Li}$ and ${}^{14}_{5}\text{B}$, and as shown in Table 2.1. Their lifetimes are 0.0085 and 0.0161 sec, respectively. To cut out those spallation events, a low energy event is rejected, if cosmic-ray muons exist within 0.15 sec before the low energy event. The dead time caused by this tight spallation cut is 36%.

6.3 summary

Table 6.1 shows the number of remaining events at each reduction step for the real data and the SN relic neutrino Monte Carlo simulation.

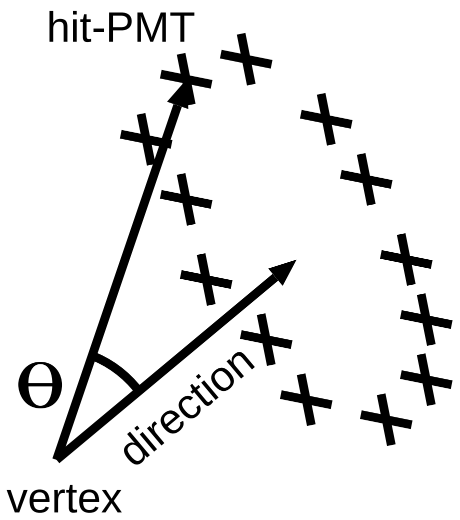

Figure 6.5: The definition of angle θ between the particle direction and the vector from the vertex to the i-th hit PMT, where the direction and the vertex are the ones reconstructed.

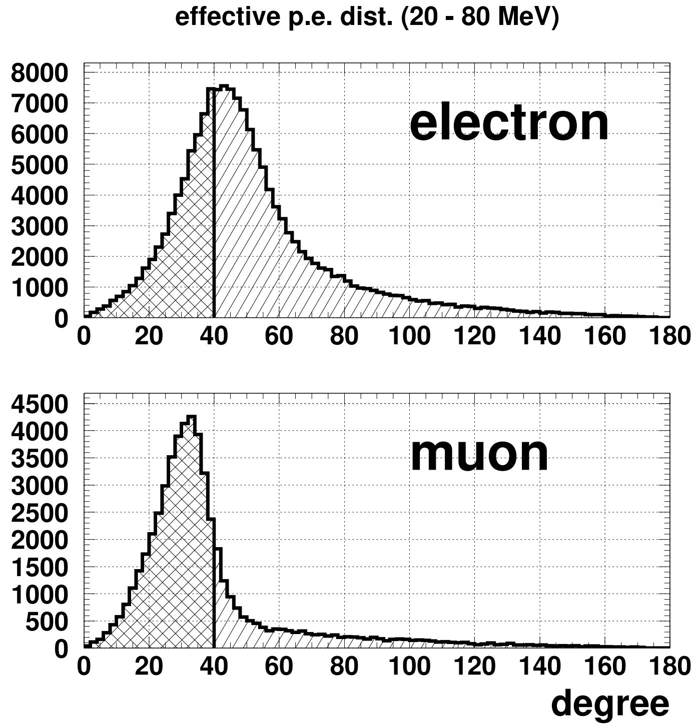

Figure 6.6: effective p.e. distribution as a function of Cherenkov opening angle

	Reduction step	Real Data	MC data	remark
first reduction	after total p.e. cut	2996678937		
	L.E. triggered	1472107178		
	after unfitted event cut	1172908227		
	after fiducial volume cut	191471131	8139	
	after time difference cut	94438892		
	after noise event cut	78522797	8121	
	after goodness cut	45144995	8121	
	after 6.5 MeV energy cut	2349644	6361	
	after spallation cut	639818		20% dead time
second reduction	after gringo cut	497803	6180	
	after patlik cut	298822	5693	
	after clusfit cut	281393	5629	
	after 14 MeV energy cut	1148	3204	
muon cut	after decay-e cut	758		
	after ratioLR cut	645	3131	
	after tight spallation cut	450		36% dead time

Table 6.1: The table of the reduction steps. 'MC data' is SN relic neutrino MC simulation within fiducial volume.

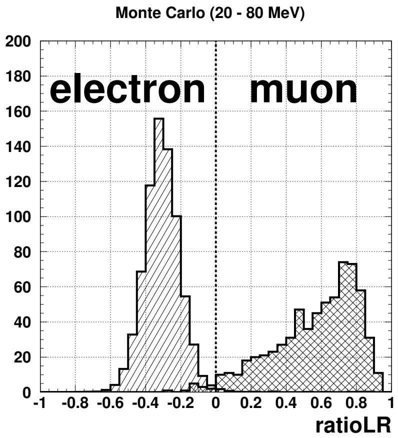

Figure 6.7: The ratioLR distributions for electrons (lined histogram) and muons (hatched histogram), made by Monte Carlo simulation.

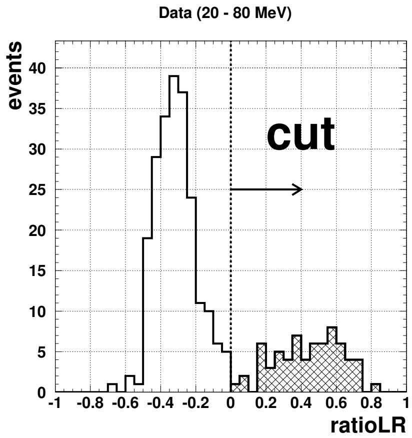

Figure 6.8: The ratioLR distributions for real events of 1260 day data sample.

Chapter 7

Monte Carlo simulation

Monte Carlo simulation gives the expectations for almost all factors: neutrino flux, interactions, particle tracking and so on. This chapter explains the methods of Monte Carlo simulation used in the Super-Kamiokande experiment.

Our Monte Carlo simulation is composed of two parts; the neutrino interaction simulation (NEUT) and the detector simulation (DETSIM). NEUT simulates neutrino interaction with water and outputs particles' data generated, that is the particle kind, vertex, direction, momentum and so on.

Those particles' data are inputed to DETSIM, which simulates particle tracking and detector response. There are two DETSIMs; APDETSIM and LEDETSIM, which are tuned for high energy particles and for low energy particles, respectively.

For atmospheric neutrino simulation, from theoretical flux, NEUT create leptons, hadrons, and γs, and those are inputed to and simulated by APDETSIM. For solar neutrino simulation, products from solar neutrinos are only electrons and its event rate is easily calculated by solar neutrino flux and neutrino cross section with water. So, we do not need to use NEUT but only use LEDETSIM. Similarly to the case of the solar neutrino simulation, products from SN relic neutrino is only positron, so we use only LEDETSIM.

7.1 neutrino interaction simulation (NEUT)

7.1.1 Atmospheric neutrino flux

Atmospheric neutrino flux has been calculated by several authors and there are several models: Honda flux [30], Bartol flux [31], Gaisser flux [32], Bugaev flux [33], and Lee Koh flux [34].

Here the flux calculated by Honda is used for atmospheric neutrino flux, because this model considers geomagnetic effect at the Kamioka site and covers the neutrino energy from 10 MeV to 1 TeV.

The uncertainty of the atmospheric neutrino flux is estimated to be 20% at 100MeV and 15% at 1-100GeV, but for the $(\nu_\mu + \bar{\nu_\mu})/(\nu_e + \bar{\nu_e})$ flavor ratio, it is estimated to be $< 5\%$ because the ambiguity in the absolute flux is cancelled out by taking the ratio.

7.1.2 Neutrino interaction

Atmospheric neutrinos interact with nucleons and electrons in water via charged current (CC) and neutral current (NC) weak interactions. However neutrino interaction with an orbital electron is negligible because the cross section with an electron is about 1000 times smaller than that with a nucleon at the energy region of atmospheric neutrinos.

For Monte Carlo simulation used in this thesis, following interaction modes are considered:

- CC quasi-elastic scattering $\nu N \to l N'$
- NC elastic scattering $\nu N \to \nu N$
- CC single-pion production $\nu N \to l N' \pi$
- NC single-pion production $\nu N \to \nu N' \pi$
- CC multi-pion production $\nu N \to l N' m\pi (m \geq 2)$
- NC multi-pion production $\nu N \to \nu N' m\pi (m \geq 2)$
- CC coherent pion production $\nu {}^{16}\mathrm{O} \to l^{\pm} {}^{16}\mathrm{O} \pi^{\mp}$
- NC coherent pion production $\nu {}^{16}\mathrm{O} \to \nu {}^{16}\mathrm{O} \pi^0$

where N represents a nucleon and l represents a charged lepton. The probability of other interaction modes including strange particle production is too small compared to the above interactions in this energy range so they are neglected. Each interaction is described below.

Quasi-elastic scattering

About 60 % of the atmospheric neutrinos of energy around 1 GeV interacts with nucleons via CC quasi-elastic scattering. For the CC quasi-elastic interaction, the energy and momentum of a lepton in the final state are determined from the q^2-dependence of the cross section. The cross section is calculated based on the standard V-A theory [26].

In the reaction:

$$\nu + n \to l^- + p \tag{7.1}$$

$$\bar{\nu} + p \to l^+ + n, \tag{7.2}$$

the Lorentz-invariant amplitude $(\mathcal{M})$ is written

$$\mathcal{M} = \frac{G_F}{\sqrt{2}} < l(p_l)|j^{\mp\lambda}|\nu(p_\nu) >< N'(p_{N'})|J^{\pm}_{\lambda}|N(p_N) >, \tag{7.3}$$

where p_ν, p_N, p_l, and $p_{N'}$ are the 4-momentum of incident neutrino, target neucleon, scattered charged lepton, and recoil neucleon, respectively,

$$< l(p_l)|j^{\mp\lambda}|\nu(p_\nu) >= \left(\begin{array}{c}\bar{u}\\ \bar{v}\end{array}\right)(p_l)\gamma^\lambda(1-\gamma_5)\left(\begin{array}{c}u\\ v\end{array}\right)(p_\nu), \tag{7.4}$$

$$< N'(p_{N'})|J^{\pm}_\lambda|N(p_N) >= \cos\theta_c \bar{u}(p_{N'})\Gamma_\lambda u(p_N), \tag{7.5}$$

$$\Gamma_\lambda = \gamma_\lambda F^1_V(q^2) + \frac{i\sigma_{\lambda\nu}q^\nu \xi F^2_V(q^2)}{2M} + \gamma_\lambda\gamma_5 F_A(q^2), \tag{7.6}$$

G_F is the Fermi's constant, $\cos\theta_c$ is the Cabibbo angle, $M = (M_p + M_n)/2$ is the nucleon mass, $\xi \equiv \mu_p - \mu_n = 3.71$ (μ = anomalous magnetic moment) and F^1_V,F^2_V and F_A are the vector and axial vector form factors expressed as:

$$F^1_V(q^2) = \left(1 - \frac{q^2}{4M^2}\right)^{-1}\left[G^V_E(q^2) - \frac{q^2}{4M^2}G^V_M(q^2)\right], \tag{7.7}$$

$$\xi F^2_V(q^2) = \left(1 - \frac{q^2}{4M^2}\right)^{-1}\left[G^V_M(q^2) - G^V_E(q^2)\right], \tag{7.8}$$

$$F_A(q^2) = \frac{-1.23}{\left(1 - \frac{q^2}{M_A^2}\right)^2}, \tag{7.9}$$

$$G^V_E(q^2) = \frac{1}{\left(1 - \frac{q^2}{M_V^2}\right)^2}, \quad G^V_M(q^2) = \frac{1+\xi}{\left(1 - \frac{q^2}{M_V^2}\right)^2}. \tag{7.10}$$

M_V and M_A are the vector and axial-vector mass and are taken to be 0.84GeV and 0.01GeV, respectively, according to Ref [27].

The cross section for this reaction is:

$$\frac{d\sigma}{dt} = \frac{|\mathcal{M}|^2}{\pi(2ME_\nu)^2} \tag{7.11}$$

$$= \frac{M^2G^2\cos^2\theta_c}{8\pi E_\nu}\left[A(q^2) \mp B(q^2)\frac{(s-u)}{M^2} + \frac{C(q^2)(s-u)^2}{M^4}\right], \tag{7.12}$$

where

$$A(q^2) = \frac{(m_e^2 - q^2)}{4M^2}\left[\left(4 - \frac{q^2}{M^2}\right)\left(F_A(q^2)\right)^2 - \left(4 + \frac{q^2}{M^2}\right)\left(F^1_V(q^2)\right)^2\right. \tag{7.13}$$

$$-\frac{q^2}{M^2}\left(\xi F^2_V(q^2)\right)^2\left(1 + \frac{q^2}{4M^2}\right) - \frac{4q^2F^1_V(q^2)\xi F^2_V(q^2)}{M^2} \tag{7.14}$$

$$\left.-\frac{m_e^2}{M^2}\left(\left(F^1_V(q^2) + \xi F^2_V(q^2)\right)^2 + \left(F_A(q^2)\right)^2\right)\right], \tag{7.15}$$

$$B(q^2) = -\frac{q^2}{M^2}F_A(q^2)\left(F^1_V(q^2) + \xi F^2_V(q^2)\right), \tag{7.16}$$

$$C(q^2) = \frac{1}{4}\left(\left(F_A(q^2)\right)^2 + \left(F^1_V(q^2)\right)^2 - \frac{q^2}{4M^2}\left(\xi F^2_V(q^2)\right)^2\right), \tag{7.17}$$

and s, t and u are the Mandelstam variables. Integrating $\frac{d\sigma}{dt}$ by t, total cross section (σ_{tot}) is given.

Figure 7.1 shows the calculated cross section and the real data in $\nu_\mu n \to \mu^- p$ and $\bar{\nu}_\mu p \to \mu^+ n$, respectively.

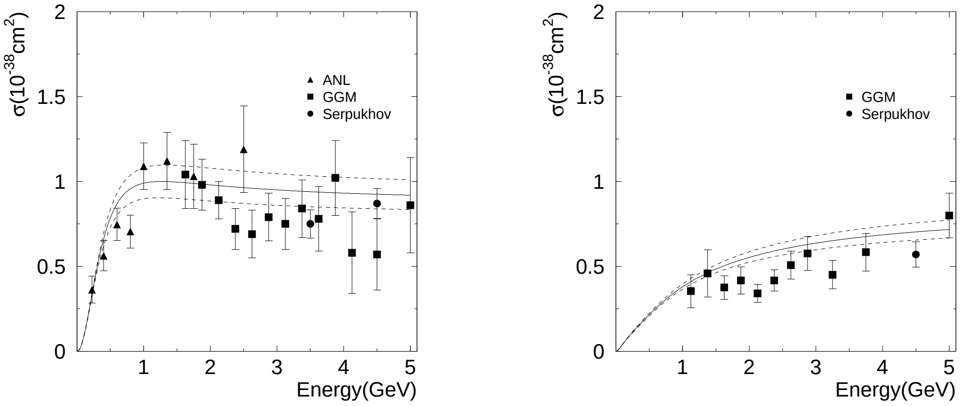

Figure 7.1: Calculated cross section of quasi-elastic interactions for $\nu_\mu n \to \mu^- p$ (left) and $\bar{\nu}_\mu p \to \mu^+ n$ (right), respectively. Calculations are compared to the experimental data: ANL [35], GGM [36], Serpukhov [37].

If the target is nucleon in Oxygen, the effects of Fermi motion and the Pauli blocking have to be considered. For Pauli blocking momentum of the recoil nucleon should exceed the Fermi surface momentum. And Fermi motion is estimated from the experimental data of e ^{12}C scattering.

In the simulation, neutral current elastic interaction is also considered, which most of them are invisible in the detector. The cross section for NC elastic scattering is estimated by the factor multiplied to CC cross sections according to Ref. [38]:

$$\begin{aligned}
\sigma(\nu p \to \nu p) &= 0.153 \times \sigma(\nu p \to e^- p), \\
\sigma(\bar{\nu} p \to \bar{\nu} p) &= 0.218 \times \sigma(\bar{\nu} p \to e^+ n), \\
\sigma(\nu n \to \nu n) &= 1.5 \times \sigma(\nu p \to \nu p), \\
\sigma(\bar{\nu} n \to \bar{\nu} n) &= 1.0 \times \sigma(\bar{\nu} p \to \bar{\nu} p). \qquad (7.18)
\end{aligned}$$

Single pion production

The single pion production is the interaction which is dominant next to quasi-elastic interaction in the energy range less than 1 GeV. This interaction are based on the Rein-Sehgal model

[39], and the interaction is calculated through the following two parts:

$$\begin{aligned} \nu + N \rightarrow \ l + \quad & N^* \\ & N^* \quad \rightarrow \ \pi + \ N' \end{aligned}$$

where N^* is a baryon resonance such as Δ. This model calculates the amplitudes of 18 resonance states. Then it multiplies the respective amplitude by the branching ratio that the excited baryon decays into one pion and a nucleon, also considering interference among the resonances. Figure 7.2 shows the total cross sections for CC and NC interactions, compared with experimental data.

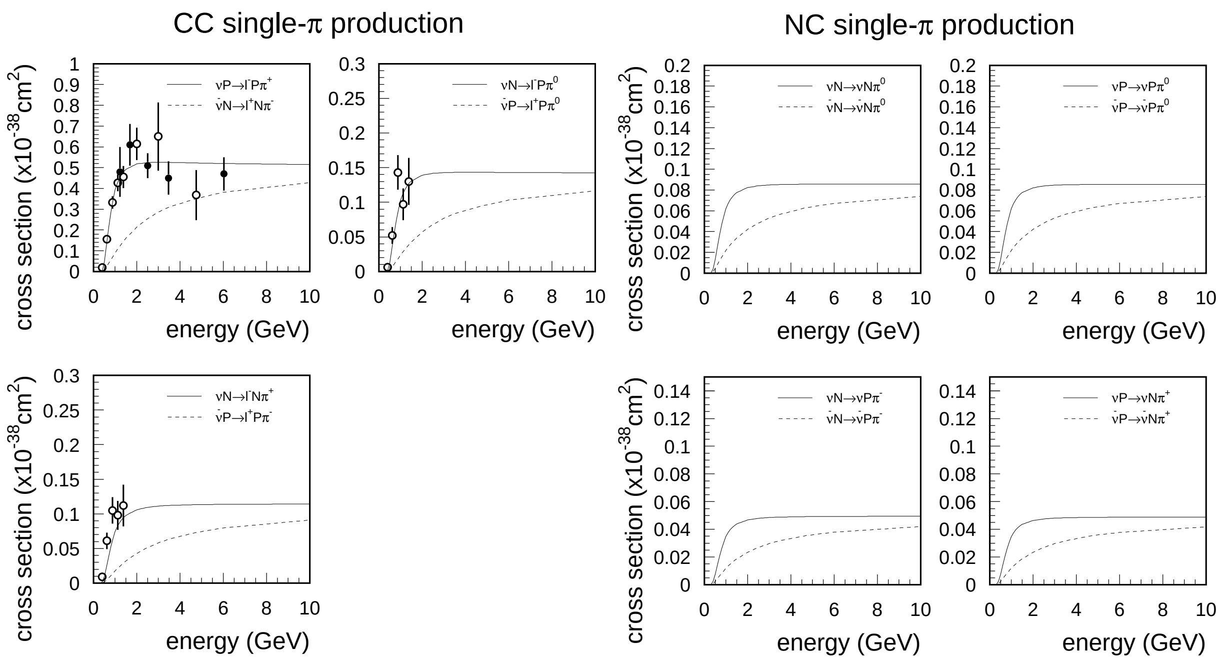

Figure 7.2: Calculated cross section of CC single-π production (left) and NC single-π production.

Multi-pion production

Multi-pion production is the interaction that produces more than one pion with the invariant mass of hadronic system W larger than 1.4 GeV/c^2. At the invariant mass region $1.4 < W < 2.0$ GeV/c^2, differential cross section can be expressed by assuming the final state hadron as pions and its multi-pion cross section as cross section of deep-inelastic scattering. The multiplicity of pions are determined from experimental data [40] as;

$$\langle n_\pi \rangle = 0.09 + 1.83 \ln W^2, \tag{7.19}$$

and three π^+,π^0,π^- are equally generated. Figure 7.3 shows the total cross section for multi pion production.

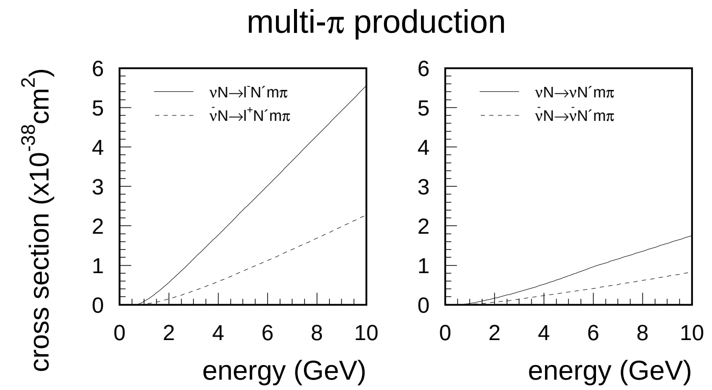

Figure 7.3: Calculated cross section of multi-π production.

Coherent pion production

Coherent pion production is a coherent interaction of neutrino with a nucleus as a whole, oxygen in water. This interaction produces one pions of the same charge as the incoming weak current. This production is characterized by an angular distribution of pion that is more sharply peaked in the forward direction than that of incoherent and resonance interactions.

The calculation of the cross section and kinematics is based on the Rein-Sehgal model [41]. Figure 7.1.2 shows the total cross section of coherent pion production of ^{16}O, for CC and NC as a function of energy.

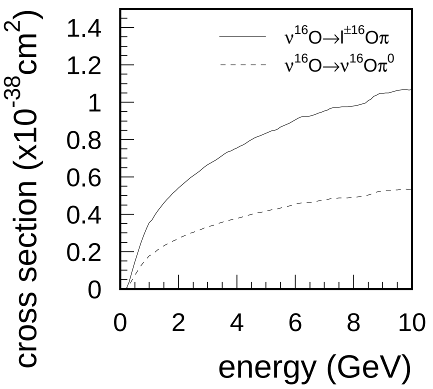

Figure 7.4: Calculated cross section of coherent π production.

7.1.3 Meson nuclear effect

Mesons, especially pions, produced in a ^{16}O nucleus often make secondary interactions before leaving the nucleus. Following three nuclear interactions for pions are taken into account: inelastic scattering, absorption, and charge exchange. For the density of the nucleus, the function of Woods-Saxon model is adopted:

$$\rho(r) = \frac{Z}{A}\bar{\rho}\left\{1 + \exp\left(\frac{r-c}{a}\right)\right\} \tag{7.20}$$

where A is the mass number, Z is the atomic number, $\bar{\rho}$ is the average density of nucleus, and $a = 0.41$fm and $c = 2.69$fm are the density parameters of nucleus. Fermi motion of nucleus and Pauli blocking effect are taken into consideration.

The calculated total cross section is shown in Fig. 7.1.3 with experimental data. Agreement is quite reasonable.

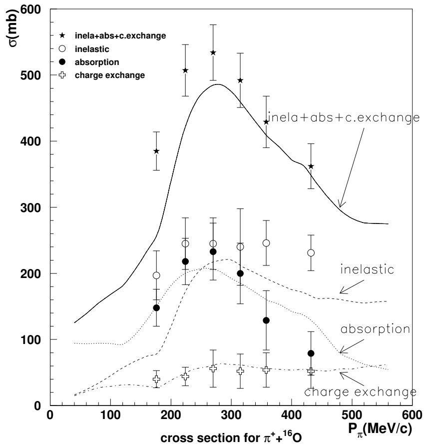

Figure 7.5: Calculated cross section of $\pi^{+}\ {}^{16}$O scattering, compared with the experimental data.

7.2 Detector simulation (DETSIM)

The GEANT[1] program is used to simulate the particle tracking and the detector response; interactions of particles, energy loss through the matter, and Cherenkov photon propagation.

For the attenuation of Cherenkov photon, Rayleigh scattering, Mie scattering, and absorption are taken into account.

The reflection and absorption at the surface of the PMTs and black sheets are included in the simulation. The characteristics of PMTs: the quantum efficiency, the dark noise, and charge and time resolution are also taken into consideration in our Monte Carlo simulation.

[1]It has been developed at CERN and commonly used in high-energy physics experiments.

Chapter 8

Backgrounds

The followings are the remaining backgrounds after reductions mentioned in Chapter 6.

8.1 Atmospheric neutrino

Figure 8.1 shows the expected number of events given by the Monte Carlo simulation (40 years exposure) after all the reconstructions and the reductions mentioned in Chapter 5 and 6. This is normalized to the real data, where livetime (1260 day) and dead time (0.36) caused by spallation cut are taken into account.

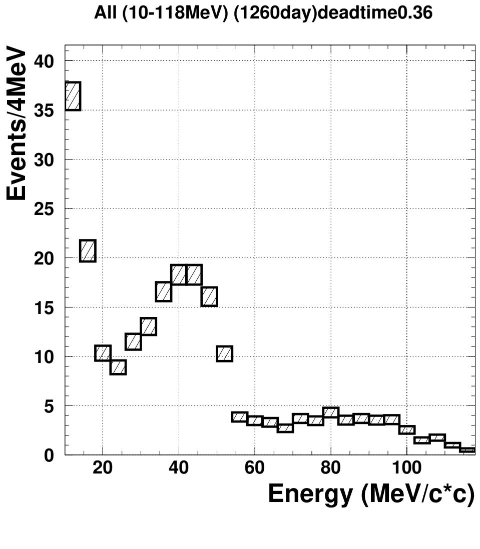

Figure 8.1: The expected number of events come from the atmospheric neutrinos, which is given by the Monte Carlo simulation (40 years exposure) after all the reconstructions and the reductions, normalized to the real data, where livetime is 1260 day and dead time is 0.36.

The decrease around 100MeV is caused by the total charge cut (< 1000p.e.). The peak around

40MeV comes from the decay electrons from invisible muons[1]. They are mainly produced by the muon neutrino reaction followed by the muon decay:

$$N + \nu_\mu \rightarrow N' + \mu(\text{invisible}) \tag{8.1}$$

$$\mu(\text{invisible}) \rightarrow e + \nu_e + \nu_\mu, \tag{8.2}$$

where N is a nucleon. Further invisible pion caused by the various neutrino reactions also cause such decay electron events, because pion decays produce muons. The decay electrons from muons obey the Michel spectrum as shown in Figure 8.2.

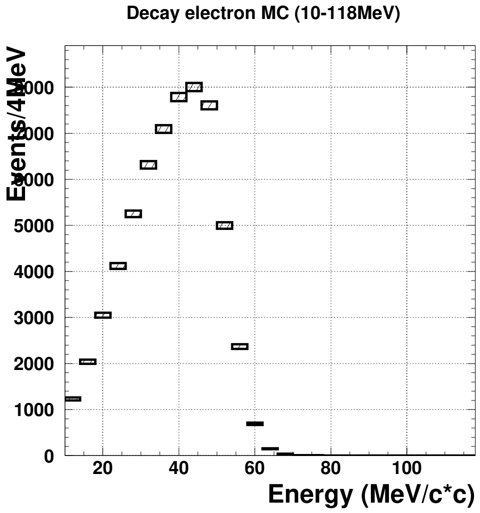

Figure 8.2: The energy spectrum of the decay electrons, which is called Michel spectrum.

Figure 8.3 shows the contamination of those types of decay electron background events more clearly. The blank histogram is the same as Figure 8.1, and the hatched histogram shows the events of such decay electrons.

The peak ($E < 20$MeV) comes from the γ-rays emitted on the de-excitation of nucleus to bury the hole made by the neutral current elastic scattering[42].

8.2 Neutrino oscillation

Figure 8.4 shows the effect of the neutrino oscillation with $\sin^2(2\theta) = 1$, $\Delta m^2 = 3 \times 10^{-3}\text{eV}^2$. There is little difference in the region $E > 60$MeV, because these events are caused by ν_e, then are not influenced by neutrino oscillation.

The difference around 40MeV peak is caused by $\nu_\mu \rightarrow \nu_\tau$ oscillation. In this energy range the oscillation lengths mentioned in Chapter 2, becomes $L_V \sim 40$km, so the downward-going

[1] See the footnote in Chapter 6.

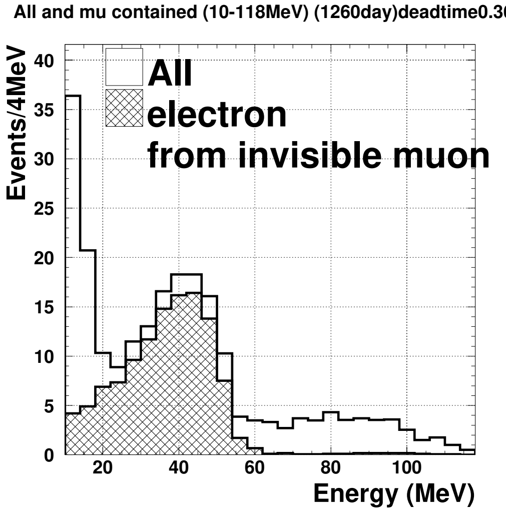

Figure 8.3: The blank histogram shows all the remaining atmospheric neutrino background, the hatched histogram shows the electron events caused by muon decay, where muons are produced by various neutrino reactions in water. Those are given by the Monte Carlo simulation (40 years exposure). It is normalized to real data.

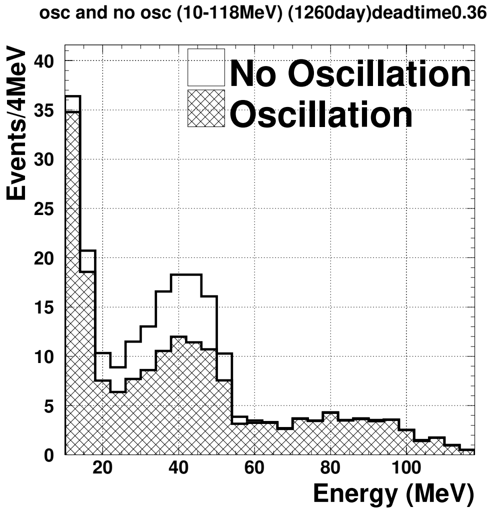

Figure 8.4: Comparison of the neutrino oscillation case with parameter of $\sin^2(2\theta) = 1$ and $\Delta m^2 = 3 \times 10^{-3}\mathrm{eV}^2$ (hatched histogram) and the non-oscillation case (blank histogram).

atmospheric neutrinos traveling $\sim$ 10km are not influenced. On the other hand, the upward-going neutrinos traveling 10^4km are fully oscillated and become one-half. Then in the case of neutrino oscillation, the number of the expected neutrinos become about 3/4 of the non-oscillation case.

Figure 8.5 shows difference among various oscillation parameters on the 90% confidence level contour map which are obtained by atmospheric neutrino oscillation analysis[28]. Difference caused by the oscillation parameters is negligible.

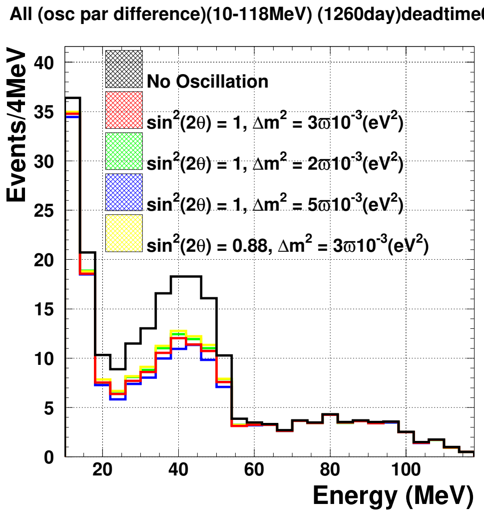

Figure 8.5: neutrino oscillation parameter depencency

Chapter 9

Analysis

Figure 9.1 shows energy spectrum of remaining events after all the reduction mentioned in Chapter 6. Almost all events are considered to come from atmospheric neutrinos.

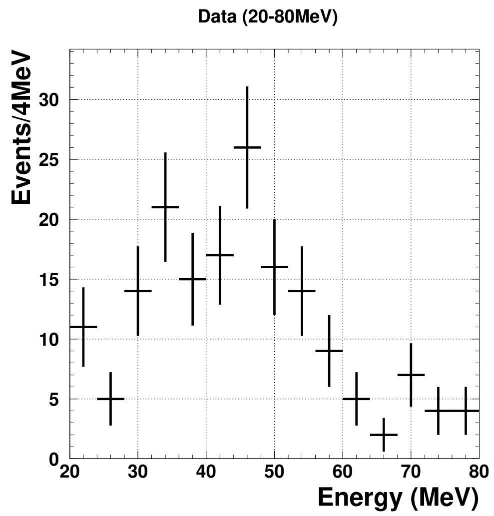

Figure 9.1: The energy spectrum of remaining events after all the reductions mentioned in Chapter 6.

Figure 9.2 shows the expected number of events given by Monte Carlo simulation of atmospheric neutrinos, taking into account of neutrino oscillation with the parameters of $\sin^2 2\theta = 1$, $\Delta m^2 = 3. \times 10^{-3}\mathrm{eV}^2$.

To obtain the number of events of the SN relic neutrinos, it is ideal to subtract the expected number of events of atmospheric neutrinos from the final data, but there is $\sim 20\%$ uncertainty in the absolute atmospheric neutrino flux. Then to remove the uncertainty of the amount of the atmospheric neutrino flux, I use a fitting method with two free parameters. The number of

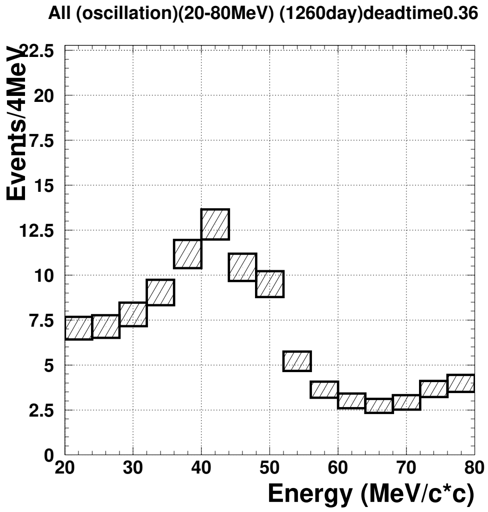

Figure 9.2: The expected number of events given by Monte Carlo simulation of atmospheric neutrinos, taking into account of the neutrino oscillation with the parameters of $\sin^2 2\theta = 1$ and $\Delta m^2 = 3. \times 10^{-3}\mathrm{eV}^2$

events of SN relic neutrinos is obtained to minimize the χ^2 value:

$$\chi^2 = \sum_{20 \le E \le 80} \frac{[(\mathrm{data})_i - \alpha(\mathrm{relic})_i - \beta(\mathrm{atm}\ \nu)_i]^2}{(\mathrm{data})_i + \alpha^2(\mathrm{relic})_i + \beta^2(\mathrm{atm}\ \nu)_i} \tag{9.1}$$

where α and β are free parameters varying $\alpha \ge 0$ and $\beta \ge 0$ region, $(\mathrm{data})_i$, $(\mathrm{relic})_i$, and $(\mathrm{atm}\ \nu)_i$ are the numbers of events of real data, of SN relic neutrino Monte Carlo (Figure 9.3), and of atmospheric neutrino Monte Carlo, respectively. For the SN relic neutrino Monte Carlo, the spectrum shape of the flux calculated by [8] is used.

χ^2 minimum value is 21.1 when the degree of freedom $n = 15 - 2 = 13$. $\chi^2/n = 1.62$. Here the number of SN relic neutrino events is 0. Figure 9.4 shows (data) and $\alpha(\mathrm{relic}) + \beta(\mathrm{atm}\ \nu)$, with the best fitted parameters.

Upper limit of the number of events of SN relic neutrinos (90 % C.L.) is 9.92. Figure 9.5 shows (data) and $\alpha(\mathrm{relic}) + \beta(\mathrm{atm}\ \nu)$, which gives the 90% confidence level upper limit of the SN relic neutrinos.

Upper limit to the total flux of SN relic neutrinos is given by the relation:

$$F_\nu \equiv \int_0^\infty f_\nu(E_\nu) dE_\nu < \frac{n_p}{N_p T \sigma \epsilon}, \tag{9.2}$$

where n_p is the number of observed events, N_p is the number of free protons (hydrogen nuclei) within fiducial volume, T is the livetime. And σ is the weighted average of the cross section given by

$$\sigma \equiv \frac{\int_{20}^{80} f_\nu(E_\nu)\sigma(E_\nu) dE_\nu}{\int_0^\infty f_\nu(E_\nu) dE_\nu}, \tag{9.3}$$

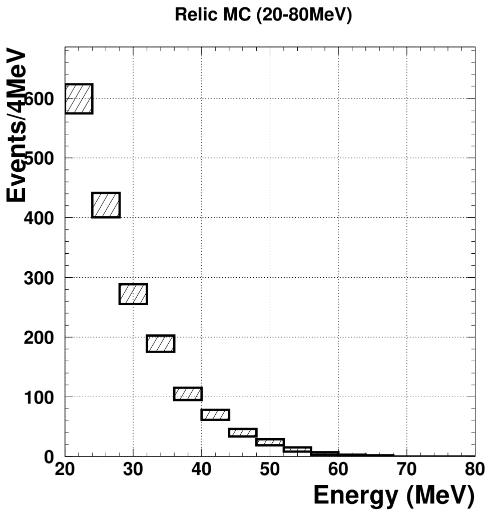

Figure 9.3: The SN relic neutrino spectrum by Monte Carlo simulation, where the flux is calculated by [8].

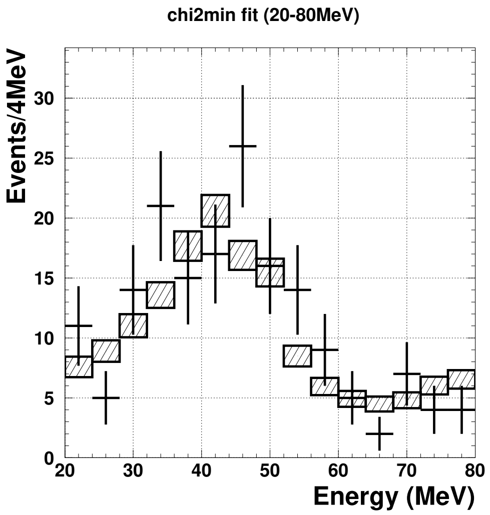

Figure 9.4: (data) and $\alpha(\text{relic}) + \beta(\text{atm } \nu)$, with the best fitted parameters.

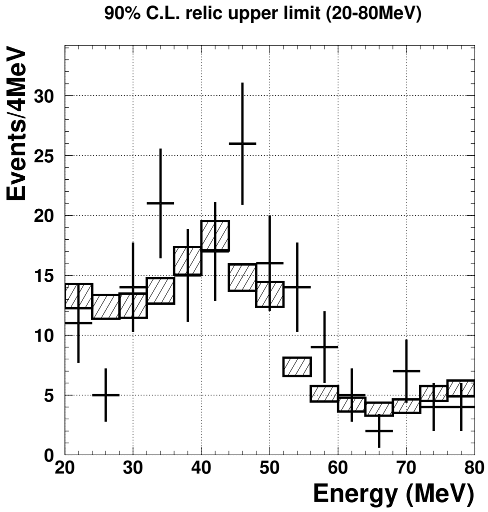

Figure 9.5: (data) and α(relic) + β(atm ν), which gives the 90% confidence level upper limit of the SN relic neutrinos.

where σ is the cross section of the reaction ($\bar{\nu_e} p \to e^+ n$), $f(E_\nu)$ is the expected SN relic neutrino flux calculated by [8]. Since there are $f(E_\nu)$s in the numerator and denominator, the absolute amount of the flux is not reflected into this value, but only the shape of the flux is reflected. ϵ is the detection efficiency for the SN relic neutrino events within 20-80 MeV, expressed by

$$\epsilon \equiv \frac{\int_{20}^{80} f_\nu(E_\nu)\sigma(E_\nu)\epsilon(E_\nu)dE_\nu}{\int_{20}^{80} f_\nu(E_\nu)\sigma(E_\nu)dE_\nu}, \tag{9.4}$$

where $\epsilon(E_\nu)$ is the detection efficiency as a function of the neutrino energy. The value ϵ is obtained by applying the reduction for the SN relic neutrino Monte Carlo simulation directly.

Inputing the following values,

$$\begin{aligned} n_p &= 9.92, & (9.5)\\ T &= 1260 \times (1 - 0.36)(\mathrm{day}), & (9.6)\\ N_p &= 1.50 \times 10^{33}, & (9.7)\\ \sigma &= 4.44 \times 10^{-43}(\mathrm{cm}^2), & (9.8)\\ \epsilon &= 0.93, & (9.9) \end{aligned}$$

the upper limit for the total flux of SN relic neutrinos is given by

$$F_\nu < 231(\mathrm{cm}^{-2}\mathrm{sec}^{-1})(90\%\mathrm{C.L.}). \tag{9.10}$$

This number is 3.4 times smaller value than so far obtained, and 5.2 times larger value than theoretically expected value.

Chapter 10

Conclusion and Future Outlook

10.1 Conclusion

Using a 1260 day sample (78 kt·year exposure) of the Super-Kamiokande detector, the SN relic neutrinos from the past supernovae are searched. After the reconstruction in Chapter 5 and the reduction in Chapter 6, we select 138 electron events in the energy range between 20 and 80MeV. On the other hand, The number of the atmospheric neutrino backgrounds is estimated by the Carlo simulation in Chapter 7. Assuming the spectrum shape in [8] as the SN relic neutrino, two parameter fitting method for the real data and the Monte Carlo simulation are used to estimate the number of the SN relic neutrinos. There are no signal events of the SN relic neutrinos. The 90% confidence level total flux limit of the $\overline{\nu_e}$ SN relic neutrinos is obtained to be $F_\nu < 231(\mathrm{cm}^{-2}\mathrm{sec}^{-1})$, which is the best value, so far. This number is 3.4 times smaller than the value so far obtained, and 5.2 times larger than the value theoretically expected.

10.2 Future outlook

To improve the limit further and to possibly discover SN relic neutrinos, the following items are to be improved.

10.2.1 Absolute flux of the atmospheric neutrino

Absolute flux of the atmospheric neutrinos must be determined definitely. For this purpose it is greatly anticipated that the absolute flux of the primary cosmic rays are observed, for example by BESS experiment.

In the energy region $E_\nu \lesssim 100\mathrm{MeV}$, the uncertainty of the absolute flux of the atmospheric neutrinos is large ($\sim 20\%$). To make this uncertainty small, 3 dimensional flux calculation must be done, because in this energy range the cosmic rays are bent by the earth magnetic field.

10.2.2 Monte Carlo

The main background for the SN relic neutrinos is the decay electrons from invisible muons, which are an inevitable background for the water Cherenkov detector. To decrease such a background, lower trigger threshold is better. Indeed, to observe lower energy solar neutrinos, the trigger threshold is lowered gradually. To deal with the change of the threshold, the Monte Carlo simulation must be the so-called *time event* which include the information of the elapsed day.

The γ-rays from the de-excitation of ^{16}O can also be a background. Simulator of this is not studied well enough, then it must be done. For this study, It is good to use the *K2K* data to investigate such neutral current reaction rates.

10.2.3 Reduction

For the energy range $10 \lesssim E_\nu \lesssim 20$MeV, the spallation background is large, The spallation cut must be studied more.

The π^-s are captured before decay, which make a sharp edge and clear Cherenkov ring. Using such feature, we can reject them, but it has not been done.

The μs and $\pi^\pm$s are sometimes scattered and make multiple clear rings, such events are remaining after the reduction in Chapter 6. The algorithm to recognize such multi rings is known as shown in [43], but it has not been applied.

10.2.4 Modifications of Super-Kamiokande

The reaction of the SN relic neutrino $\bar{\nu_e}$ in water is followed by the neutron capture as follows:

$$\bar{\nu_e} p \rightarrow e^+ n, \tag{10.1}$$

$$np \rightarrow d\gamma(2.2\text{MeV}), \tag{10.2}$$

where the neutron capture reaction occurs about 200 μsec after. This correlation can be used for detecting the SN relic neutrino events. The advantage of this method is that it does not depend on the atmospheric neutrino background. But, there are two difficulty to realize this method: one is that the background event rate is high, and the other is that the detection efficiency for the 2.2 MeV γ-ray is low. The background event rate might become about 7 kHz within the fiducial volume for 2 MeV threshold. Now, we are making effort to reduce the radon background. If this project proceeds successfully, the background is reduced to <10%. Using the program modified slightly, the detection efficiency for the 2.2 MeV γ-rays are investigated. The result is 13.5%. Even if low background (event rate < kHz) is realized, the upper limit of the total flux for the SN relic neutrinos is $F_\nu < 1000$ cm^{-2}sec^{-1} by 3 year-observation, because the detection efficiency is too low. We must develop a new algorithm to get 2.2 MeV γ-ray more efficiently.

It is a good strategy to put NaCl into the tank. The reaction below is expected:

$$\bar{\nu_e} p \rightarrow e^+ n \tag{10.3}$$
$$n^{35}\mathrm{Cl} \rightarrow \gamma^{36}\mathrm{Cl}, \tag{10.4}$$

where a positron event of a $\bar{\nu_e}$ is followed by a γ-ray event, whose energy is 8.6MeV then can be observed by good efficiency. This correlation can be used for the signal of the SN relic neutrinos.

In this case, there are no background mentioned above, however there is possibility that new elements Na and Cl cause new backgrounds, for example, new spallation products. We must study about backgrounds more. For the realization of dissolving salt, we must develop the facility of a new water purification, or desalination system. Furthermore, other matters must be studied.

Bibliography

[1] K. Hirata *et al.*, Phys. Rev. Lett. **58**, 1490 (1987)

[2] K. S. Hirata *et al.*, Phys. Rev. D **38**, 448 (1988)

[3] R. M. Bionta *et al.*, Phys. Rev. Lett. **58**, 1494 (1978)

[4] M. Kaplinghat, G. Steigman, T. P. Walker, Phys. Rev. D **62**, 043001 (2000)

[5] D. H. Hartmann, S. E. Woosley, Astropar. Phys. **7**, 137 (1997)

[6] R. A. Malaney, Astropar. Phys. **7**, 125 (1997)

[7] T. Totani, K. Sato, Int. J. Mod. Phys. D **5**, 519 (1996)

[8] T. Totani, K. Sato, Y. Yoshii, Astrophys. J. **460**, 303 (1996)

[9] T. Totani, K. Sato, Astropar. Phys. **3**, 367 (1995)

[10] S. E. Woosley, J. R. Wilson, R. Mayle, Astrophys. J. **302**, 19 (1986)

[11] A. Dar, Phys. Rev. Lett. **55**, 1422 (1985)

[12] P. O. Lagage, Nature **316**, 420 (1985)

[13] L. M. Krauss, S. L. Glashow, D. N. Schramm, Nature **310**, 191 (1984)

[14] G. S. Bisnovatyi-Kogan, Z. F. Seidov, Ann. N. Y. Acad. Sci. **422**, 319 (1984)

[15] J. N. Bahcall, T. Piran, Astrophys. J. **267**, L77 (1983)

[16] J. N. Bahcall, Astrophys. J. **216**, L115 (1977)

[17] K. S. Hirata, Ph. D. Thesis, Univ. of Tokyo (1991)

[18] W. Zhang *et al.*, Phys. Rev. Lett. **61**, 385 (1988)

[19] H. Suzuki, "Physics and Astrophysics of Neutrinos", edited by M. Fukugita, A. Suzuki, Springer-Verlag (1994) p. 763

[20] M. Takahara, !VAT@dJk@1$N;`!W, G]Iw4[(1994)

[21] H. Suzuki, F|K\J*M}3X2q;o **Vol. 43, No. 2**, 106 (1988)

[22] R. Mayle, J. R. Wilson, D. N. Schramm, Astrophys. J. **318** 228 (1987)

[23] J. Arafune, M. Fukugita, Phys. Rev. Lett. **59**, 367 (1987)

[24] W. C. Haxton, Phys. Rev. D **36**, 2283 (1987)

[25] P. Vogel, J. F. Beacom, Phys. Rev. D **60**, 053003 (1999)

[26] C. H. L. Smith, Phys. Rep. **3**, 261 (1972)

[27] K.L.Miller *et al.*, Phys. Rev. **D26**, 237 (1982).

[28] T. Kajita, Y. Totsuka, ICRR-Report-463-2000-7 (2000)

[29] Y. Totsuka, "Physics and Astrophysics of Neutrinos", edited by M. Fukugita, A. Suzuki, Springer-Verlag (1994) p. 625

[30] M. Honda *et al.*, Phys. Rev. D **52**, 4985 (1995).

[31] P. Lipari, T. K. Gaisser and T. Stanev, Phys. Rev. **D58**, 073003 (1998).

[32] T. K. Gaisser, T. Stanev, G. Barr, Phys. Rev. D **38**, 85 (1988)

[33] E. V. Bugaev and V. A. Naumov, Phys. Lett. **B232**, 391 (1989).

[34] H. Lee and Y. Koh, Nuovo Cimento B **105**, 884 (1990).

[35] S.J.Barish *et al.*, Phys. Rev. **D16**, 3103 (1977).

[36] S.Bonetti *et al.*, Nuovo Cimento **A38**, 260 (1977).

[37] S.V.Belikov *et al.*, Z. Phys. **A320**, 625 (1985).

[38] K.Abe *et al.*, Phys. Rev. Lett. **56**, 1107 (1986).

[39] D.Rein and L.M.Sehgal, Ann. of Phys. **133**, 1780 (1981).
D.Rein, Z. Phys. **C35**, 43 (1987).

[40] S.J.Barish *et al.*, Phys. Rev. **D19**, 2521 (1979).

[41] D.Rein and L.M.Sehgal, Nucl. Phys. **B223**, 29 (1983).

[42] H. Ejiri, Phys. Rev. C **48**, 1442 (1993)

[43] M. Shiozawa, Ph. D. Thesis, Univ. of Tokyo (1999)